



UNIVERSITAT POLITÈCNICA DE CATALUNYA
BARCELONATECH
Escola d'Enginyeria de Barcelona Est

BACHELOR FINAL PROJECT

Biomedical engineering degree

**RNA EXPRESSION ANALYSIS AND QUANTIFICATION FROM
IMAGES DURING LIMB REGENERATION**



Memory & Annex

Autor/a: Enrique Franky Vargas
Director/a: MUÑOZ ROMERO, JOSE JAVIER
Co-Director/a: COMELLAS SANFELIU, ESTER
Call: June 2023

Resumen

Este trabajo implementa una metodología para analizar la expresión de los morfogenes, que son moléculas o factores que actúan como señales químicas fundamentales en el desarrollo de un organismo, y son esenciales para la formación de patrones en la biología. Estos morfogenes están presentes en imágenes de LFSM (microscopía de lámina de fluorescencia por luz) obtenidas durante el proceso de regeneración de la articulación sinovial del Axolotl, capturadas mediante la técnica de HCR FISH (Cadena de Reacción de Hibridación Fluorescente in situ, por sus siglas en inglés), con el fin de cuantificar y medir los principales patrones de concentración. Para lograrlo, se utilizan las herramientas proporcionadas por las aplicaciones de análisis de imágenes en el entorno MATLAB, en conjunción con la teoría relacionada con el análisis de imágenes de fluorescencia y los fundamentos de las imágenes biológicas. El objetivo principal es establecer un marco de referencia para los modelos propuestos en la predicción de patrones de Turing en la regeneración celular.

Resum

Aquest treball implementa una metodologia per analitzar l'expressió dels morfògens, que són molècules o factors que actuen com a senyals químiques fonamentals en el desenvolupament d'un organisme i són essencials per a la formació de patrons en la biologia. Aquests morfògens estan presents en imatges de LFSM (microscòpia de làmina de fluorescència per llum) obtingudes durant el procés de regeneració de l'articulació sinovial de l'Axolotl, capturades mitjançant la tècnica de HCR FISH (Cadena de Reacció d'Hibridació Fluorescent in situ, per les seves sigles en anglès), amb la finalitat de quantificar i mesurar els principals patrons de concentració. Per aconseguir-ho, s'utilitzen les eines proporcionades per les aplicacions d'anàlisi d'imatges en l'entorn MATLAB, en conjunció amb la teoria relacionada amb l'anàlisi d'imatges de fluorescència i els fonaments de les imatges biològiques. L'objectiu principal és establir un marc de referència per als models proposats en la predicció de patrons de Turing en la regeneració cel·lular.

Abstract

This work implements a fundamental methodology to analyze the expression of morphogens, which are molecules or factors that act as fundamental chemical signals in the development of an organism and are essential for the formation of patterns in biology. These morphogens are present in images obtained through LFSM (Light Sheet Fluorescence Microscopy) during the regeneration process of the synovial joint in Axolotls, captured using the HCR FISH technique (Fluorescent In Situ Hybridization Chain Reaction), with the aim of quantifying and measuring the main concentration patterns. To achieve this, the tools provided by image analysis applications in the MATLAB environment are used in conjunction with the theory related to fluorescence image analysis and the fundamentals of biological images. The main objective is to establish a reference framework for the proposed models in the prediction of Turing patterns in cellular regeneration.

Acknowledgments

I want to thank my mom for always being there and making it possible for me to pursue this international double degree. Her love and support mean the world to me. I'm also grateful to my friends and classmates who have been with me on this journey, making learning easier and more enjoyable. To my teachers and mentors, thank you for your guidance and knowledge that have helped me reach this point. In short, to all of you, your support has been crucial in my success in this program, and I'm deeply grateful for it.

INDEX

RESUMEN	2
RESUM	3
ABSTRACT	4
ACKNOWLEDGMENTS	6
PREFACE	9
Background	9
Motivation.....	9
1. INTRODUCTION	11
2. OBJECTIVES	14
3. METHODOLOGY	15
3.1. Preprocessing	16
3.1.1. Structure of images – Z stack.....	16
3.1.2. Uploading image information and metadata properties to MATLAB workspace.	16
3.1.3. Pyramidal resolution	20
3.1.4. Blur and point spread function.	20
3.1.5. Background subtraction.....	23
3.1.6. Noise	24
3.2. Processing	26
3.2.1. Histogram analysis.....	26
3.2.2. Binarization.....	27
3.2.3. Morphological operation	29
3.2.4. Segmentation.....	31
3.3. Post – processing	33
3.3.1. Selection of parameters and segmented pattern.	33
3.3.2. Measure original properties.	33
4. RESULTS	35
DISCUSSION	39
Global reference	39
Parametrization	40

CONCLUSIONS	41
ECONOMIC ANALYSIS	42
AMBIENTAL IMPACT	43
BIBLIOGRAPHY	45
ANNEX	48
Results for different filter values	48
Day 14 post amputation	48
Day 15 post amputation	50
Day 17 post amputation	52
Day 18 post amputation	54
Day 21 post amputation	56
Day 26 post amputation	58

Preface

The focus of this study is derived from the repository of Final Degree Projects (TFG) at Universitat Politècnica de Catalunya Escola d'Enginyeria de Barcelona Est (UPC-EEBE). This project serves as the culmination of my biomedical engineering degree and showcases the proficiencies attained throughout the academic curriculum, coupled with my international experience from Colombia. This endeavour takes place during the program's ultimate semester, after the completion of all prescribed courses, thus ensuring the acquisition of requisite knowledge and competencies for the execution of professional research in the realm of biomedical science. Specifically, this undertaking resides at the crossroads of molecular biology and image processing.

Background

This project originated from a collection of whole-mount images captured using light sheet fluorescence microscopy (LSFM), displaying the chemical signals within a regenerating axolotl forelimb. These LSFM images were obtained at Northeastern University in Boston, United States, as part of the co-director's postdoctoral research initiative. Both supervisors are engaged in an ongoing research endeavor within their group, aiming to construct a predictive computational model for joint formation based on regrowing axolotl forelimbs. These LSFM images play a pivotal role in informing this model.

Consequently, there arose a requirement to formulate a methodology for the analysis and quantification of chemical signal expression within the three-dimensional space at various timepoints during the regeneration process. This analysis was conducted using MATLAB to facilitate the incorporation of this information into the predictive model. The images under consideration comprise a volumetric stack of two-dimensional representations, depicting the expression of specific molecules integral to the regrowth of amputated forelimbs over several days, constituting a regenerative process.

Motivation

In the study conducted by (Tahar, et al 2023), they developed a predictive patterning model using reaction-diffusion systems, which are commonly employed to investigate pattern formation in biological systems. They combined this approach with linear stability analysis and finite element modelling of a Turing system featuring Schnakenberg kinetics. The objective was to examine the impact of initial conditions and the expansion of domains on the competition among permissible modes in the emergence of 3D Turing patterns. The outcomes of their research provided fresh insights into the mechanisms that ensure reliable pattern formation in 3D spaces. These insights hold significance for

developing more robust models for morphogen patterning – the process of chemical signalling guiding developmental procedures.

Pattern formation is a critical step in morphogenesis, a concept introduced by Alan Turing to explain how cellular signalling can generate self-organizing patterns (Turing 1952). These patterns drive the differentiation of cells and their organization into distinct tissues and structures. The transition from 2D to 3D reaction-diffusion systems introduces a wider array of patterns. Given the widespread utilization of Turing systems for modelling various biological scenarios and their alignment with experimental observations, these Turing patterns aid in comprehending the emergence of specific natural patterns.

The Turing system offers a valuable framework for understanding pattern genesis in diverse morphogenetic processes, often linked with growing structures. Analysing the emergence of Turing patterns within developing 3D domains offers insights into the contributing factors and circumstances in morphogenesis. The researchers initiated an exploration into the influence of initial conditions and growth on simple 3D Turing patterns. Their goal is to model the patterns of morphogen expression encountered during development.

An essential consideration when employing Turing-based systems to model morphogenesis is their robustness. The utilization of Turing patterns to investigate morphogen expression is widely adopted in developmental biology (Manini et al 2012). Investigating the origination of patterns and their dependence on domain size evolution is particularly pertinent to comprehending processes like limb formation. Integrating computational modelling of Turing patterns with experimental evaluations of morphogen expression promises a better understanding of morphogen patterning and a deeper comprehension of the mechanisms underpinning these processes.

1. Introduction

The ability of living beings to generate fully differentiated tissues and structures is present during the gestation or embryonic stage. However, this capability is mostly lost after birth, except for a few organisms that retain some level of regeneration capacity and those that undergo metamorphosis, in which case it is rather the embryonic development of new structures. While regeneration can still occur after birth, it is primarily focused on healing and repair rather than full restoration of damaged tissues or structures as they were before. This phenomenon is observed across complex organisms, including humans, except for a small group that can regenerate specific structures even after birth and development. There are several research groups that aim to gain a deeper understanding of the underlying mechanisms and pathways that regulate this capacity, with the goal of expanding our knowledge and uncovering new insights that could have important implications for the medical field. The axolotl salamander (*Ambystoma mexicanum*) is among one of the most studied animals to this aim. The regeneration capacity present in the axolotl is not unique as all the tetrapod amphibians, especially the tailed salamanders, have it in different degrees. The reason why the axolotls and the newt specimens are the most studied animals regarding this is that they their regeneration capability can regrow amputated limbs as they were the (Simon & Tanaka 2013). The study models generated from their analysis help us to understand better the molecular and cellular processes that promote this capacity. There are several stages across the process as well as mechanisms and factors that drive the regeneration capability: nerve supply of the region, epidermis and healing processes, limb bud formation, molecular and cellular signalling pathways, blastema and blueprint formation, and epigenetic factors (Simon & Tanaka 2013). Numerous signalling pathways have been studied in limb regeneration, and some growth factors and signalling pathways demonstrate to have a direct inhibitor effect on the regeneration process, which suggests a fine equilibrium between the promotion and suppression of the regeneration (Chijimatsu & Saito 2019). Aside from this inhibition effect, there are other effects of interest which affect the size and functionality of the regenerated limb, as it must be regulated to stop growing once the regenerated limb is fully formed (Wells, Baumel y Mccusker 2022). This regulation is done by a process denominated “ontogenetic allometric growth”, where the limb growth is related to the rest of the body. Another effect that is still under study is the capability of the cells and tissues to retain some identifying information about the position, structure, and patterns of the previous (Simon & Tanaka 2013). The size of the injury itself has a non-trigger response on the regenerative capacity. To obtain more understanding on this complex global process it is important to research in different stages of the animal development, as some modulations of the growth factor are preserved from embryonic development.

This work will focus on the spatial patterning generated by the expression of specific morphogens, which are genetically-regulated molecular biomarkers that coordinate key events of morphogenetic

processes like in joint formation, in the different stages of formation of a regenerated synovial joint. This biological structure has distinctive methods regarding the mechanisms and signalling pathways of regeneration involved. As it must develop unique highly specialized tissues such as articular cartilage and undergo a special process of bone rudiment separation known as cavitation, it is a complete field of study in the regeneration research (Chijimatsu & Saito 2019). One important particularity is the generation of a region named interzone, which marks the origin of the joint. This region is responsible of the segmentation of skeleton elements in the limbs (through cavitation) and can be recognized by the representative expression of the morphogen growth differentiation factor 5 (GDF-5). Mutations on this gene cause skeletal malformations and therefore it is suggested that it is essential for healthy joint development, as it mediates in the generation and maintenance of the interzone. The interzone precedes the cavitation event, and after the bone rudiment separation appears the articular cartilage is developed in the synovial joint by joint morphogenesis. In this event recent studies suggest that extracellular matrix is filled by a compound fluid, in which the principal component is the hyaluronic acid. Movement, muscular contraction and myogenesis (i.e., differentiation of muscle cells) have essential roles across the cavitation process and in the development of healthy joints.

The establishment of the skeletal limb structure occurs through a series of phases. In the initial stages, two morphogen types cooperate to locate the future joint site by promoting chondrocyte differentiation beyond the interzone. This collaboration is illustrated by Growth Differentiation Factor 5 (Gdf-5) and its counterpart NOGGIN. Following this, morphogens in the interzone facilitate bone rudiment separation, contributing to joint formation. Finally, a regulatory loop controlling cell proliferation and hypertrophy shapes the ultimate size and configuration of elongated bones.

The GDF-5 has a chondrogenic effect in the interzone, related to the chondrogenesis process that is required in the formation of mineralized skeleton in vertebrates (Brendan F. , Michael J. & Lianping 2018), in conjunction with the expression of *bone morphogenic protein 2 and 4* (BMP4 & 5) signalling. Once specialized the region, NOGGIN and Chordin proteins regulate negatively the chondrogenic (and osteogenic) effect by binding directly to the morphogens GDF-5, BMP4 and BMP5. Thus, NOGGIN contributes to the joint formation by antagonizing the chondrogenic effect of GDF-5.

As a direct part of chondrogenesis regulation, the SOX genes affect the limb size and their main transcription factor SOX9 is considered the master chondrogenic factor in embryonic limb development. Therefore, and due to the observations and experiments realized with mutations of these genes, transcription factors of these family are considered to have importance on the regulation of growth during limb development (Wells, Baumel & Mccusker 2022).

In (Lovely et al., 2022), scientists employed Light Sheet Fluorescent Microscopy to study the behavior of these morphogens during Axolotls' limb regeneration. They observed and recorded the expression of these molecules as they were involved in joint formation. This expression data is then intended to

be analyze in order to generate a biological framework that can be used as reference in comparisons to models about predictions in joint formation.

2. Objectives

The goal of this study is to map the 3D location of critical joint formation morphogens during axolotl limb regeneration. To this aim, a methodology must be developed to obtain quantitative measures of NOGGIN, Gdf-5 and Sox9 morphogen expression and their precise spatial position from the available wholemount LSFM images in regenerating axolotl forelimbs.

3. Methodology

The starting point are the wholemount light sheet microscopy fluorescence images taken following to the HCR-FISH protocol (Lovely et al. 2022) developed at the Monaghan Lab in Northeastern University (Boston, US). First, each image must be read, and its data uploaded into the MATLAB workspace to start the processing. As they were provided in the original manufacturer format of the microscope (Carl Zeiss s.f.), the use of Bio formats library (Linkert , et al. 2010 May 31) is needed. Alternatively, they can be converted into TIFF format with the help of image processing tools like Fiji (Schindelin et al. 2012) to continue. Once the file is read, the bio formats library can help to extract metadata about the capture conditions and parameters of the microscope used. With this information, the visualization application is created in MATLAB according to the size of the voxels. Also, with the help of wavelength2rgb function (Hofmann 2023) the colour assignment is correlated to the emission wavelength of each channel. Images have three flat channels, firstly containing SOX9 expression, secondly with Gdf-5 and the third one with NOGGIN. This information is uploaded by splitting the channels into separate matrixes to process one by one. Once each channel has been uploaded to the correspondent matrix, operations and transformations are then applied by MATLAB image processing toolbox. The following process is going to make principal use of this toolbox as well as others in the image processing and computer vision applications of MATLAB. All functions used to develop the proposed methodology will be specified in the following.

The methodology will be developed in MATLAB (The MathWorks, Inc. 2023) and consist in the following steps:

- Upload information
 - Extract metadata from the image.
 - Construction of visualization application.
 - Splitting channels.
- Processing of the LSFM image:
 - Contrast enhancement
 - Deconvolution
 - Background subtraction
 - Smooth filtering
 - Noise filtering
 - Image alignment
- Quantification of morphogen expression present in the LSFM image:
 - Thresholding and segmentation to identify 3D morphogen patterning.
 - Identification of a reference for comparison across samples
 - Quantification of shape, volume, intensity, etc. of the identified pattern
 - Mapping of spatial position of the identified pattern with respect to the bone rudiment.
 - Parametrization of the identifies 3D pattern surface.

3.1. Preprocessing

3.1.1. Structure of images – Z stack

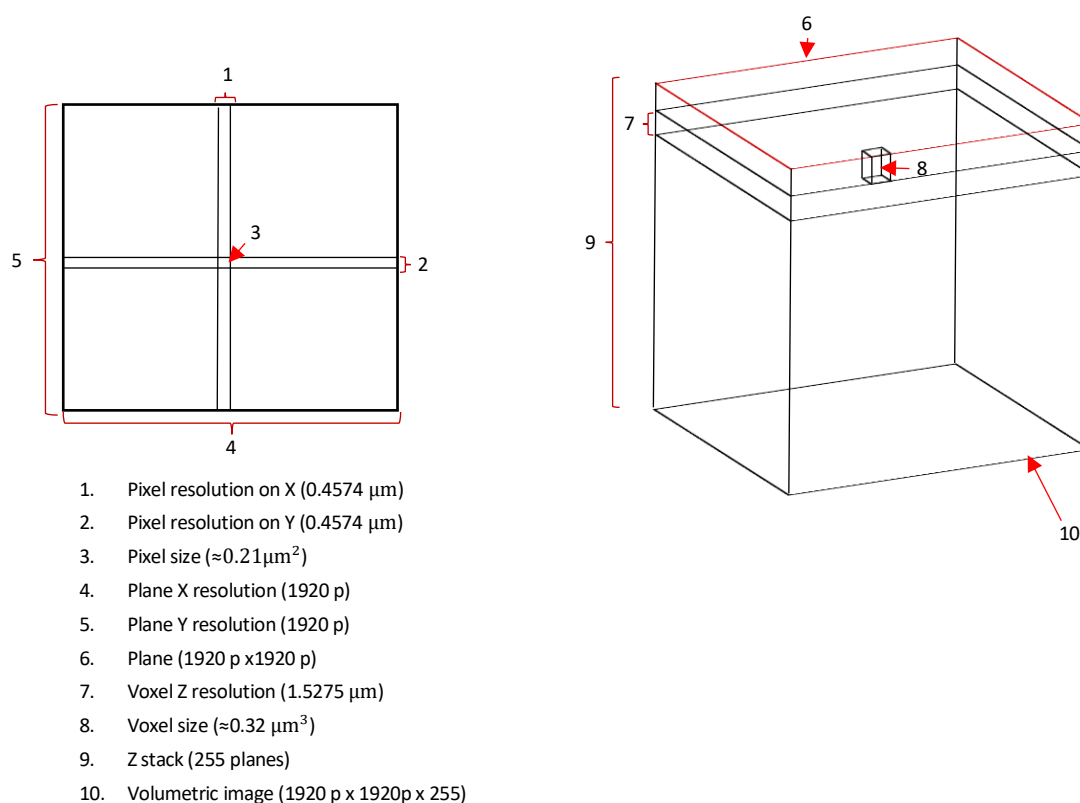


Diagram 1 : Diagram of the image stack's structure.

Diagram 1 illustrates the structure and resolution from the 17-post amputated day *z-stack* image of one single channel of morphogen expression. Each channel within the image has the same structure and resolution, and this is represented in MATLAB as a matrix as 2^{16} bits that represent unsigned intensity values (0-65535). Pixel resolution dimensions and the planes on the z stack are extracted from the metadata and are not the same on all images.

The following steps are developed for the methodology proposed:

3.1.2. Uploading image information and metadata properties to MATLAB workspace.

For reference, we can get the image visualization given by software manufacturer ZEN Lite (ZEISS ZEN Lite. s.f.), which also has functions available for pre-processing. In [Figure 1](#), on the left is the original

information as it is read it from the file that has the expression of SOX9, GDF-5 and NOGGIN taken on a 17 dpa (days post amputation) axolotl forelimb, and on the right is the same image with auto contrast applied using ZEN Lite.

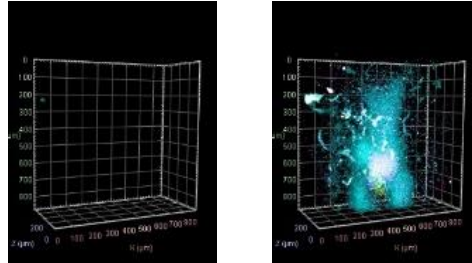


Figure 1: *Noggin (magenta), Gdf-5 (yellow) and Sox9 (cyan) expression in a 17 dpa axolotl forelimb.*

As it is observed in [Figure 1](#), the channels are mixed, and the expression of each morphogen is overlapped. To get the pattern of each expression we need to split the channels to see them individually as shown in Figure 2.

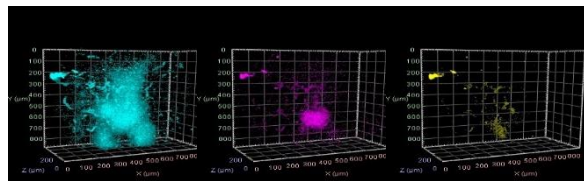


Figure 2: *Day 17 after amputation image, Sox9 (cyan), NOGGIN (magenta) and Gdf-5 (yellow) splitted.*

Firstly, we need to achieve this in MATLAB to begin the image analysis and processing. This is done first by making a 3D visualization interface accordingly to the metadata information where the original information and subsequent transformations will be displayed (see Figure 3).

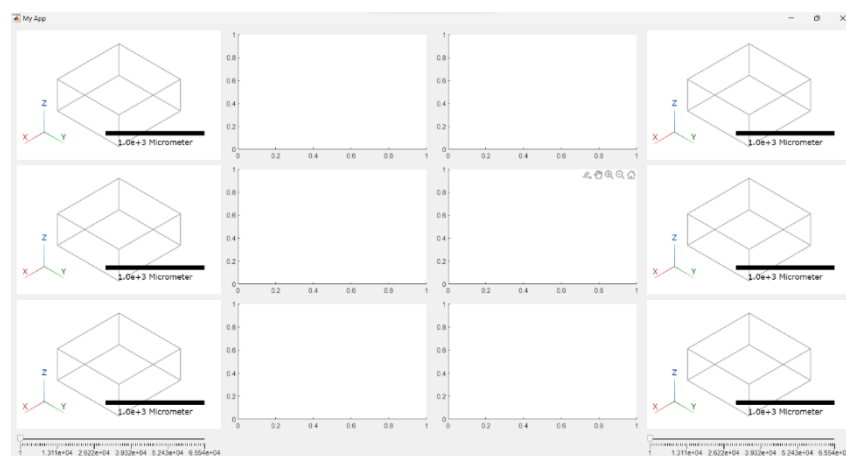


Figure 3: *Visualization interface.*

Each plane of morphogen expression is then read in separately by the bio formats library (Linkert , et al. 2010 May 31) function *bfGetPlane* and stacked into three matrixes: SOX9, GDF-5 SOX9 and with dimensions accord to the metadata. Then, each expression is adjusted by the function *imadjustn*, which also applies the function *stretchlim* underline to calculate the lower and upper limits from the image to use as contrast. What this does is that the histogram is stretched to saturate the 1% bottom and 1% top of the pixel's values present to optimize the dynamic range in the image. This is a linear operation made on pixel values to obtain contrast enhancement.

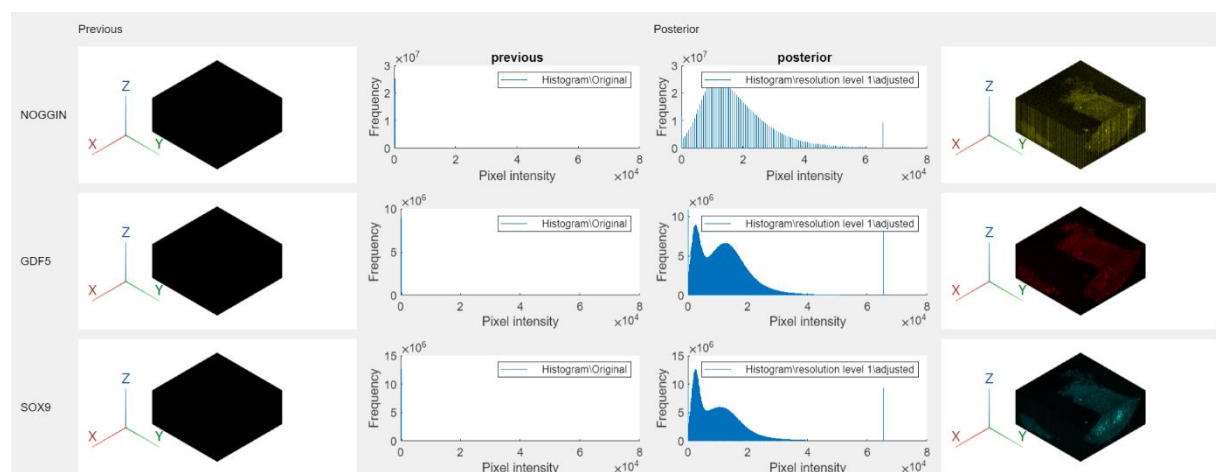


Figure 4: Original and adjusted expressions shown in Matlab for a 17 dpa limb. The complete volumetric image stack is shown.

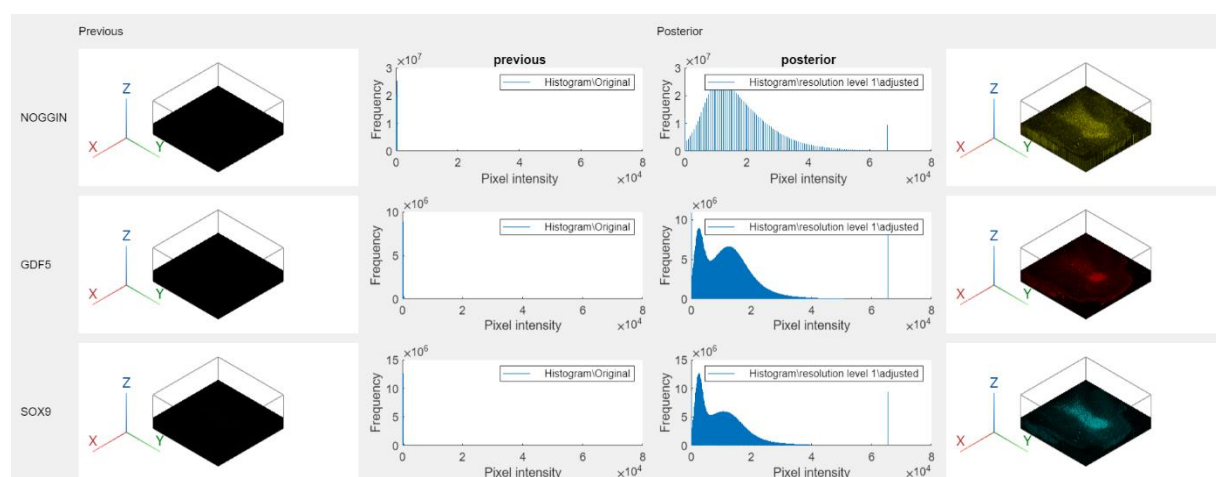


Figure 5: Original and adjusted expressions shown in Matlab for a 17 dpa limb. A longitudinal section view of the volumetric image stack is shown

Figure 4 and Figure 5 show the original information on the left for the three expressions: NOGGIN above, GDF-5 middle and SOX9 at the bottom, and their histograms on the next columns. At the right part of the figure, the expressions are contrasted and shown in the same order, with their histograms on the left column next to them. As it can be observed there are pixels with low intensity, and even

some appear to be completely black in the background. In reality, these pixels had captured some intensity of light as they are not on a true ground level (0 intensity value), but it does not mean that they correspond to the fluorescent reaction of the morphogen expression in these sites. The real ground level is not displayed in the volume as it is interpreted with no information by the 3D viewer object. This effect could correspond to the diffraction of light (Swift & Colarusso 2022), whose visual effect is illustrated as an airy disk pattern in Figure 6, not desirable for our analysis as our focus is on the patterns formed by the higher concentration of morphogen expression only.

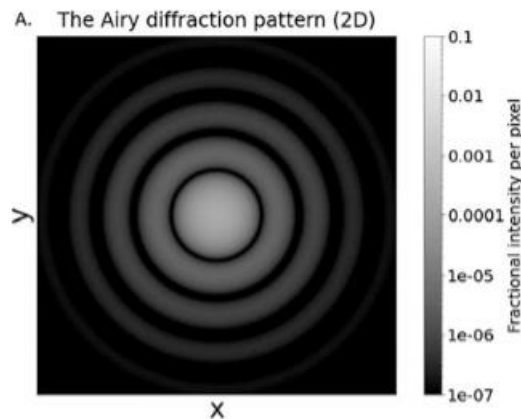


Figure 6: Diffraction pattern of light (Swift y Colarusso 2022).

It was necessary to convert the matrixes that hold the pixel information of the image expressions (NOGGIN, GDF-5, SOX9) as intensity values into *blockedImage* objects, to display the entire volume in the 3D viewer as the computational resources available in the graphics card were not enough to process the complete raw volume data. This *blockedImage* object is an image made from discrete blocks that facilitates the processing of images too large to fit in memory and with high computational cost. In this case, the discrete blocks were initially set to be an octave of the size of the planes X and Y and the same size of the plane Z. This was done because it is recommended to process blocks between 300- and 500-pixels of size, and it also made the numbers of pixels on each dimension of the block similar, which facilitates posterior filter operations. But this block partition results in aberrations on the final image as the limits of each block are seen on the final pattern. However, performance enhancement was notable and the possibility to select block size is left as an option. To overcome this problem, a single discrete block with all the image sizes is used in this methodology. Alternatively, with the adapter property of the *blockedImage* object, it is possible to make virtual stacks of the image, reading the block's data from the disk instead of having all data upload in-memory. Parallel processing is also available with some virtual stack format options. In this methodology virtual image is generated by the binary formats adapter which facilitates parallel process and save the block in an external disk.

3.1.3. Pyramidal resolution

The *blockedImage* object facilitates the creation of multiresolution images by generating scale levels of resolution from the original image while maintaining the size. This flexibility allows for the selection of a specific resolution level to apply algorithms and conduct further processing. Opting for lower resolutions brings advantages such as faster and more efficient processing due to the reduced number of pixels. However, this comes at the cost of losing pixel information and detail, potentially impacting the accuracy of algorithms and analysis. Nonetheless, the overall performance and applicability of the method are significantly enhanced by this capability, rendering it a valuable tool for image manipulation and algorithm development. The implementation is done on a 50% of resolution for the morphological and segmentation process due to limitations in the computational resources.

As it can be observed on Figure 7, the patterns formed from the agglomeration of morphogen expression present on the original image are maintain respect to the lower resolution image, so they can be extracted from there.

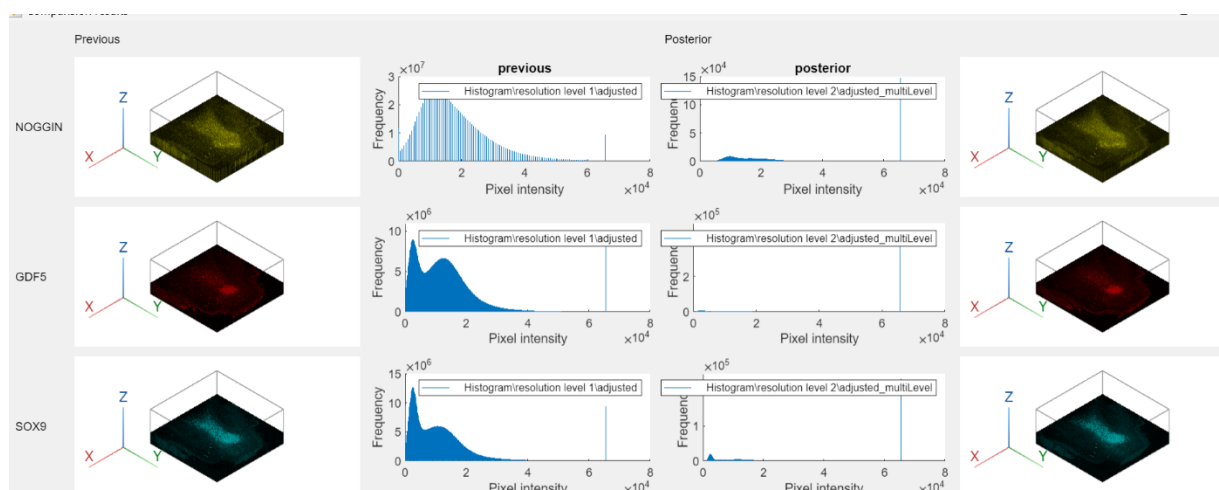


Figure 7: Original resolution on left and 50% resolution on right of longitudinal slice view.

3.1.4. Blur and point spread function.

As starting point for analyzing the images, it is necessary to understand what is represented by the pixel information captured from the fluorescent microscopy image, and how it can be interpreted as the fluorescent reaction of the morphogen's expression. In general, fluorescent images are made from the detection of a small amount of light emitted from fluorescent molecules (fluorophores) associated to non-fluorescent molecules when they get excited through a source of light. The fluorophores emit photons across a photophysical process named fluorescence. So, the most that this type of image can tell is how much light was emitted from any point on the capture space. From this information the interpretations are made relative to the non-fluorescent molecules, in this case the morphogen

molecules, according to each channel where each one was captured at different wavelengths of light as they must measure the photons emitted by different fluorescent molecules. But by no means the images are a direct representation of the non-fluorescent molecule, they are just a measure of the photons that it was possible to detect in the capture space. However, the concentration of photons can relate to the concentration of fluorescent molecules, as they emerge from them, and each fluorescent molecule is supposed to be associated with one correspondent morphogen molecule. It is in the photon detection that most of the problems of microscope images are, as the photon does not have a deterministic trajectory to the detector, and the conversion of light to electrical signals may induce errors, noise and artifacts (Bankhead 2014).

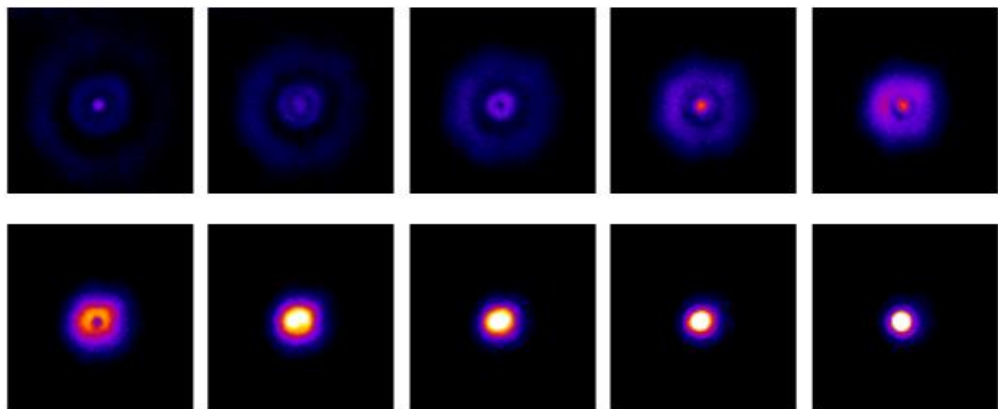


Figure 8: Effect of the out-of-focus light on ten slices of a z-stack image of a fluorescent beam, seen from above the focal plane (Bankhead 2014).

Figure 8 shows the diffraction of light of a beam over ten slices on a z-stack image. From Figure 9, it becomes apparent that variations in intensity levels on a single slice may arise by a conjunction of the diffraction of light and the defocused light from adjacent slices within the stack.

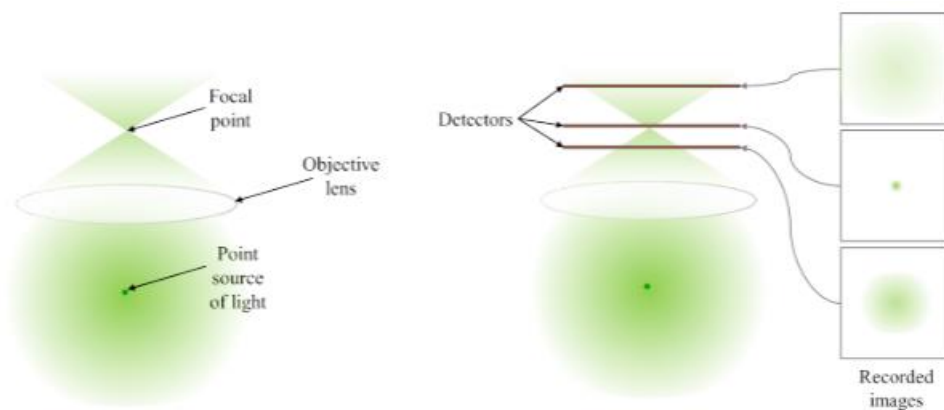


Figure 9: Simplified diagram of light emitting from a point to help visualize the effect of out of focus (Bankhead 2014).

(Lovely et al. 2022) have developed the method used to capture the images to be analyzed in this study, and all the specification of how these images were taken are in their work. This work intends to extract the information of morphogen expression from the images, and for that purpose the images are analyzed with respect to the literature available on fluorescent images processing. In 2014, (Bankhead 2014) authored a book focused on the analysis of fluorescent microscopy images using ImageJ (Schindelin et al. 2012), which has gained significant recognition due to its widespread citation by numerous researchers to this day. According to his work two critical artifacts affects the fluorescent images: the blur and the photon noise. The blur corresponds to the empirical error of the photon detection, as the photon is not detected by only one pixel and is rather spread over several pixels and cannot be focused back to a single point. This artifact causes uncertainty in space. The photon noise is also caused when the image is blurred because the photon trajectory is itself random, as mentioned before, and causes random variations in brightness throughout the image as noise. This causes uncertainty in brightness. There can be other artifacts, such as the conversion of light to electrical signals, but this section is going to treat the blur artifact.

The blur affects the apparent sizes, intensities, and structures interpreted in an image. But it is an artifact that is well understood and is not a random effect. The blurring is mathematically described by a convolution involving the microscope's point spread function interpreted as an involuntary linear filter applied at the registration of the photons, and therefore before noise artifacts, so offer no noise reduction benefits (Bankhead 2014). Since all the pixels are blurred accordingly to the *PSF* – point spread function – of the light microscope that had capture the images, it can be characterized throughout the entire image. But in the case of the morphogen expression's fluorescent images, they do not have a *PSF* associated to them, and therefore they cannot be deconvolved with it to obtain the clean registration of photons and in-focused images.

In order to solve this problem related to the light's physics nature, the *deconvblind* function was implemented on the morphogen expression images, as this function can approximate the in-focus image and the *PSF* from an initial *PSF* estimation and consequent iterations over the image by the maximum likelihood estimation algorithm. This is a highly computational task, and since its purpose is to achieve the approximation of the in-focus image and the construction of the *PSF* from the analysis of the image itself, the use of a low-resolution scale will not make sense as full information present in the original image is desirable. The restauration of the *PSF* is affected more by the size of the initial *PSF* rather than the values in it, so this method allows different scales of XY planes as initial *PSF*'s.

Figure 10 shows the optimal approximation obtained through the application of the *deconvblind* function, leveraging the constructed Point Spread Function (*PSF*) outcome. While initially holding promise, this approximation's efficacy is limited in accurately extracting the desired pattern or cleaning it. Subsequent analysis, facilitated by the *imabsdiff* function to quantify the absolute difference

between two images, reveals that the utilization of the deconvblind-derived approximation yields no alterations to the image.

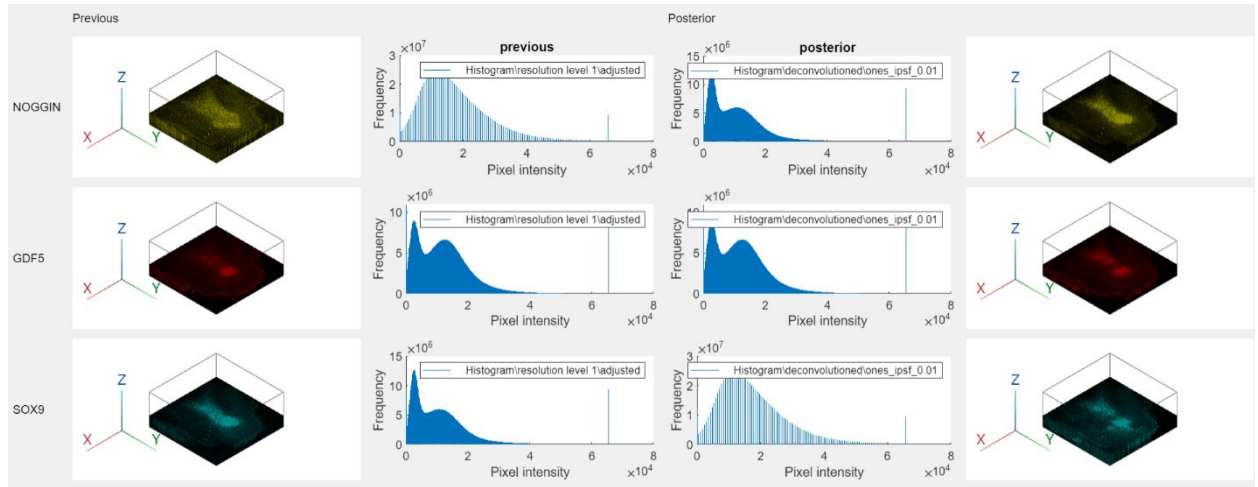


Figure 10: Deconvblind function applied to each expression (right) and corresponding original image (left).

3.1.5. Background subtraction.

An effective technique for mitigating the influence of irregular background pixels, characterized by varying brightness levels, involves the utilization of image subtraction of the median filtered image. By implementing this filter, pixels exhibiting intensity values that lie outside the spectrum of being sufficiently dark to be categorized as background or excessively bright to qualify as genuine expression are systematically eliminated on the median filtered image. The process of subtraction of this median image from the non filtered selectively retains high extreme values pixels within the resultant image. Moreover, this approach offers an additional advantage in facilitating subsequent global thresholding procedures, notably enhancing the discernment and localization of focalized spots showcasing morphogen expression patterns.

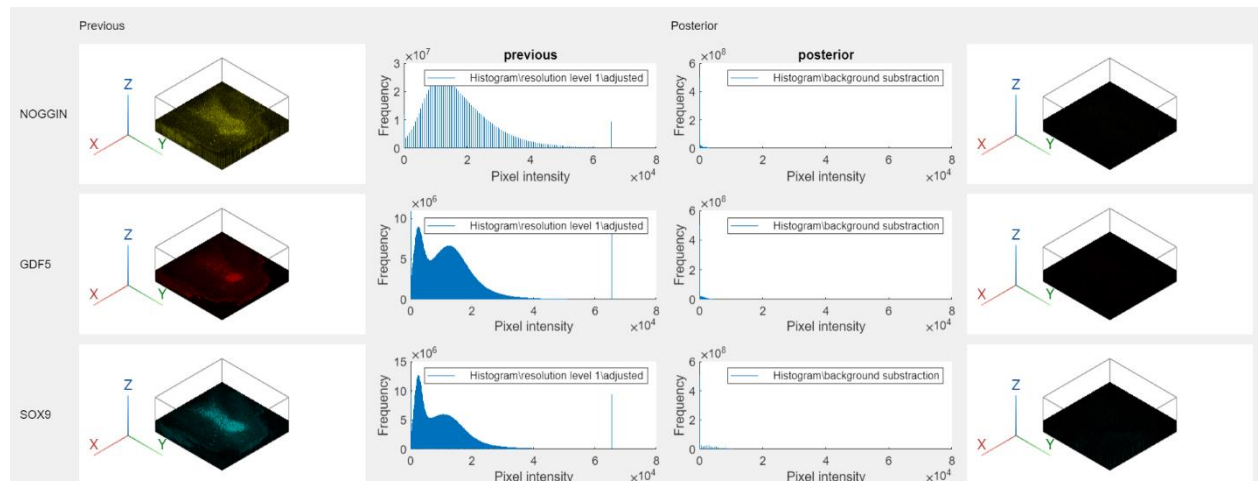


Figure 11: Background subtraction by median filter of size 10 pixels on x, 10 pixels on y and 10 planes on z (right).

In Figure 11, is the process involves subtracting the median-filtered images from their corresponding adjusted counterparts. As observed, the changes on the histogram are due to the difference of the

median corresponding values with the non filtered ones and the result is an histogram cut and condensed into lower intensity values, because all the values are lowered by a median intensity value that fitted on the filter operator region. Intensity values that initially were lower of this value are replace with true ground level (real background level, because on an image can not exist negative intensity values) and higher values are replaced by brightness intensity values accordingly by the difference. This computational operation results in a noticeable dimming of the overall expression within the images. However, it is essential to acknowledge that this approach is not without limitations. The size of the median filter employed plays a pivotal role, and in scenarios where the filter becomes saturated due to the presence of a continuous and intense region of genuine expression, the approach inadvertently eliminates authentic patterns from the data. While a potential remedy could involve employing a larger median filter, it is important to note that such a strategy carries a substantial trade-off, significantly impacting the overall performance and computational efficiency of the process.

3.1.6. Noise

Noise on a fluorescent image has three characteristics: randomness, independence and distributed by a probable density function. The main sources of noise on a microscopy image are the dark noise, originated from electronics, noise generated by thermal agitation of electrons, photon noise and readout noise. The dark noise is reduced by coolers on high-quality sensors, meanwhile the other sources of noise are inherent in all optical signals and the non-perfectness conversion between light and electrical signals. These types of noise have been modelled for microscope image denoising, as each one follows a Gaussian or Poisson distribution, and the image is the result of adding these signals to the noise-free information within the image (Bankhead 2014) (Meiniel, Olivo-Marin y Angelini 2018).

3.1.7. Gaussian noise

This model corresponds to the readout noise and has equal probability to appear throughout the entire image as the standard deviation of the distribution stays the same. Smoothing s this type of noise as it lowers the standard deviation of the distribution and increments the signal-to-noise ratio. The result is less noise present in the image, at the cost of a little loss of detail. As the size and weight of the smoothing filter increments, more detail from the image can be lost and more noise is reduced. There does not appear to be a great source of this type of noise in the morphogen images, as it is seen as granulates over the image. With the exception of some NOGGIN expression channel on images, as it is the channel with the higher potence required for the wavelength of light captured. A gaussian filter was then implemented using *imgaussfilt3* and different values for its sigma parameter were tested. The gaussian filter performs better in general in smoothing images compared to the averaging filter, which takes the mean value within the region of the filter operator, since it considers more relevant (weights) the closer pixels than the distant ones for the pixel operation in the operator region. Also, with the gaussian filter, the edges of any shape or pattern are better preserved.

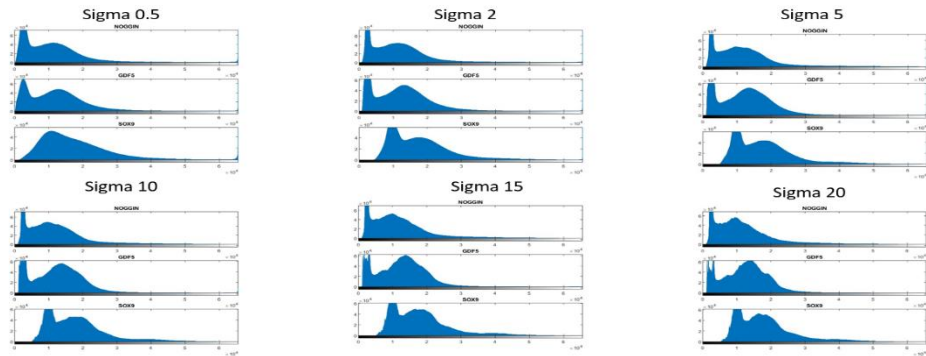


Figure 12: Histogram of different gaussian filtered images.

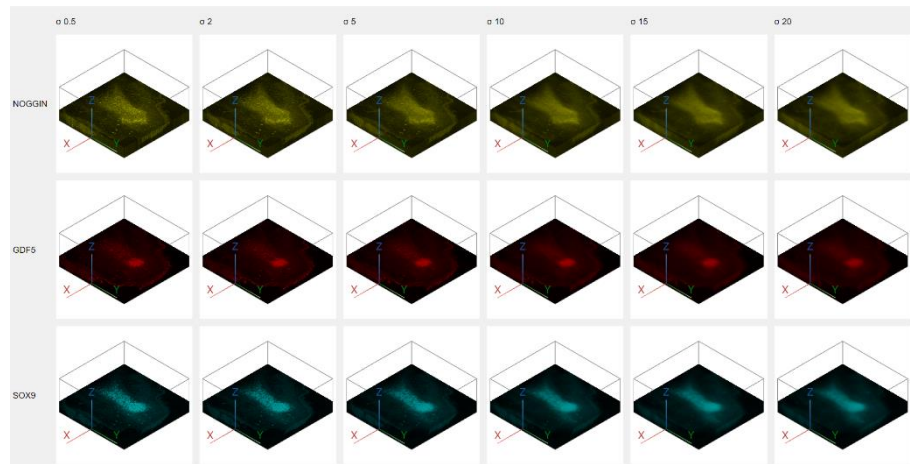


Figure 13: Different sigma parameters on Gaussian filter.

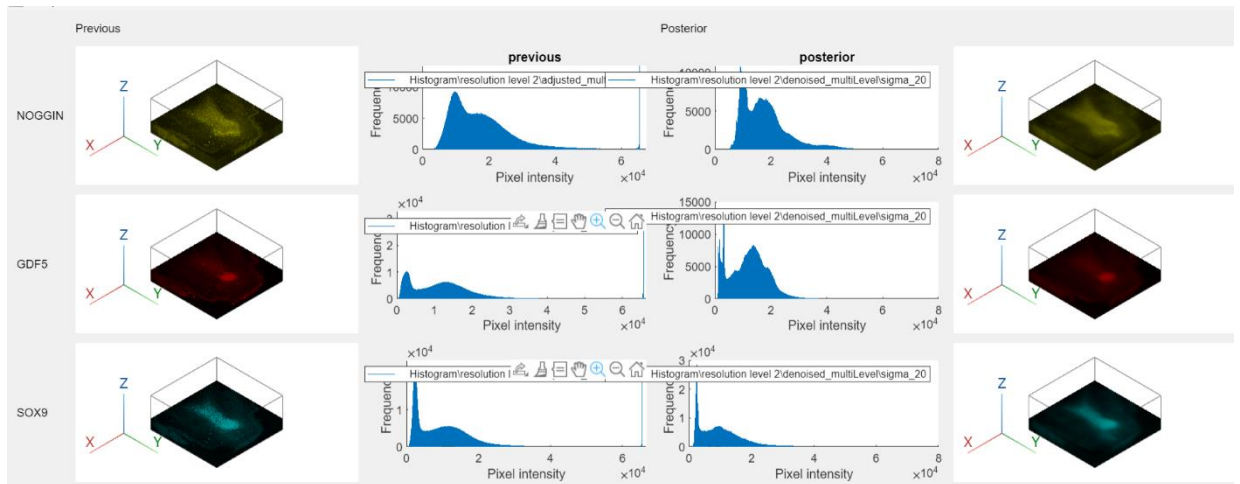


Figure 14: Smoothing by Gaussian filter on each expression. longitudinal view.

As evident from Figure 13, weight exert a more pronounced effect, effectively reducing the prominence of minor undesired objects within the images. In Figure 12 the distinction of pikes in the histograms are stronger as the sigma value increase, an even some emerges in NOGGIN channel where

there was not before. Figure 14 shows a comparison of a low sigma (right) with the non-smoothing image (left).

3.1.8. Poisson noise

This noise model corresponds to the photon noise and its probability can change accordingly to the local brightness in the image, but it can be reduced also with the smoothing of the image done on gaussian noise. But since its nature is different as the photon noise is the difference between the number of photons captured in the image, or in other words the photons emitted on the captured space, and the real rate of emission present from the excited fluorophores (Bankhead 2014), the only solution to reduce this type of noise is to detect more photons in the image (longer exposition times). However, there is not an observable factor from the morphogen images that suggest there is not enough detected photons already in the images.

3.1.9. Other types of noise

In addition to the noise models that characterize the principal sources of error inherent to the capture of light, there are other artifacts more related to the biological sample's preparation and exposure times. The auto fluorescence (Swift y Colarusso 2022) is an event from the biological sample that causes the fluorophores to emit photons even when they are not associated with the non-fluorescent molecule target (other molecules such as antibodies can associate with them) when they get excited at the moment of capturing the image. This is labeled as false expression later at the segmentation stage and excluded from the analysis as it forms a pattern that does not have the volume measure enough to be misinterpreted as the principal concentration of morphogens.

Photo bleaching is the photochemical destruction of the fluorophores after undergoing consecutives cycles of imaging process, occasioning that the fluorophores no longer emit photons. This type of noise is not present in the (Lovely, y otros 2022) images as each plane in the image stack has a different z position and therefore different fluorophores are observed.

3.2. Processing

3.2.1. Histogram analysis

Once the images have been pre-processed and smoothed by different sigma parameters their histograms are analysed to estimate different thresholds on the intensity levels. In this work, *findpeaks*, along *interp1* and *movmean* functions, are implemented to trace a continuous smooth curve approximation of the histogram discrete distribution and determinate the valley and peak thresholds.

Also, the Otsu method (Otsu 1979) is implemented by *otsuthresh* to find the threshold that maximizes the between-class variance while minimizing the within-class variance. Otsu method is automatically implemented from the histogram counts and aims to minimize the intra-class variance of pixel intensities in the resulting binary image, effectively separating the foreground and background regions. It is a widely used algorithm in image processing for object segmentation techniques. Furthermore, the 75th and 90th quantiles from the histogram counts are localized and their position on intensity level are taken as thresholds, and finally the 90th percentile of the intensity levels (2^{16} bits) are also compared as an extreme threshold. All these threshold methods are implemented on the histograms of each image and each morphogen, and illustrate as a reference mode on Figure 15.

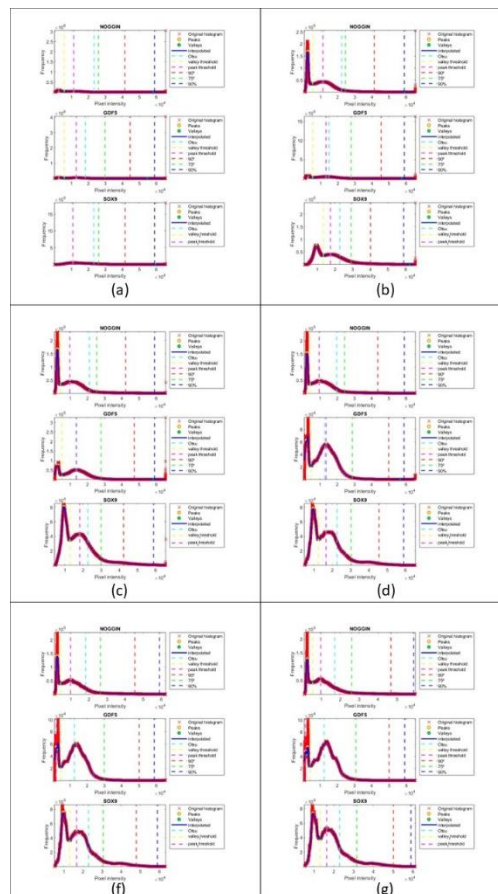


Figure 15: Thresholds applied from the histogram analysis. a) 14 days post amputation. b) 15 days post amputation. c) 17 days post amputation. d) 18 days post amputation. f) 21 days post amputation. g) 26 days post amputation.

3.2.2. Binarization

In total six different binarization thresholds were tested for segmentation with each sigma parameter value of the smoothing function, giving in total 108 image segmentation patterns, 36 for each

morphogen. The binarization operation was implemented by *imbinarize* function applied by *apply* object function of *blockedImage*.

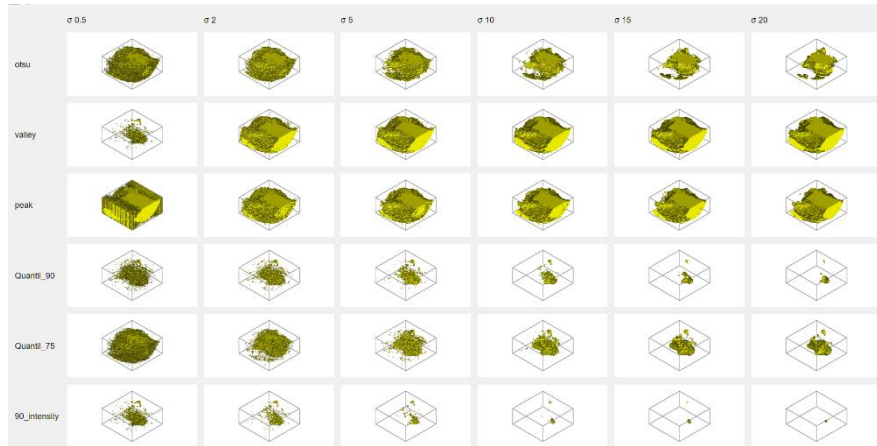


Figure 16: NOGGIN binarization of different thresholds.

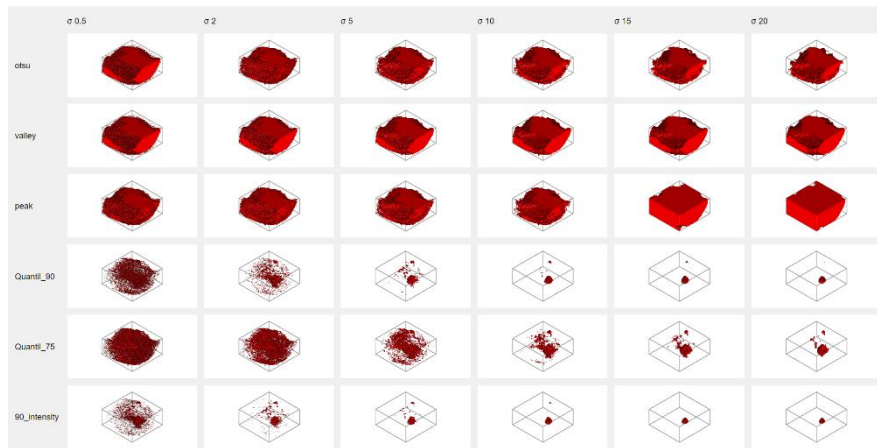


Figure 17: GDF-5 binarization of different thresholds.

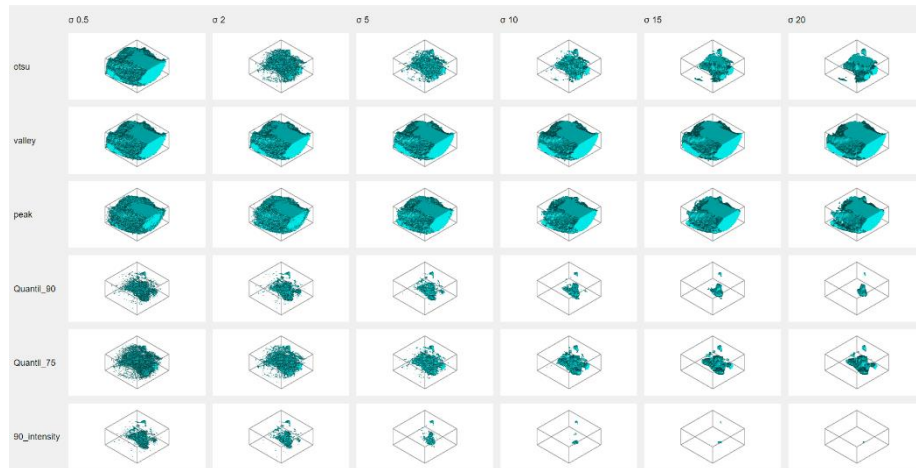


Figure 18: SOX9 binarization of different thresholds.

Figure 16, Figure 17 and Figure 18 shows the binarization results of NOGGIN, GDF-5 and SOX9 respectively for the thresholds Otsu, valley, peak, 90th, 75th and 90% on the rows and smoothing sigma values of 0.5, 2, 5, 10, 15 and 20 on the columns. The best fit of parameters for the inside pattern exhibition on this image (17 days post amputation) are threshold of 75th and sigma value of 20, and this is certain for the three channels of expression. It is important to consider the same parameters for the three channels within the same image.

3.2.3. Morphological operation

The binary image does not contain only the pattern formed from the principal expression, as some expression patterns are also formed aside the principal one and are preserved after the filtering. Also, any expression can be detected disaggregated from the rest and generate undesirable small patterns around. To fix this, morphological operations and techniques should be applied on the patterns detected as the images no longer are in intensity values. Initially, the application of the *imclose* function using a small-scale operator executes a closing operation on volumetric images. This operation effectively establishes connections between proximate expression patterns, leading to an enhancement in pattern connectivity. This heightened connectivity subsequently refines the interlinking and continuity among patterns within the image, thereby fostering greater coherence and improved discernibility. Next, the function *bwareaopen* serves to effectively eliminate patterns within the image that possess areas smaller than a predetermined fixed parameter. Consequently, the binary image undergoes a refinement process, systematically purging these smaller-scale patterns. This strategic purification procedure culminates in the preservation of the more prominent and substantial patterns, ultimately fostering a clearer and more pronounced representation of the underlying structures.

Inherent within the original image, patterns may contain voids, and the extent of their retention depends on several crucial factors. The sigma pattern embedded within the smoothing filter, the

dimensions of the close operator employed in morphological processes, and the predefined area parameter collectively influence the preservation of these voids. A potential avenue to rectify this issue lies in the utilization of a *fill* operation, closely related to the *bwmorph3* function. This operation holds the promise of obliterating the voids, thereby enhancing pattern cohesiveness. However, it is imperative to note that the application of the function necessitates an antecedent segmentation of the pattern in which it would be applied. It is essential to underscore that while the fill operation contributes significantly to the enhancement of pattern consistency, its implementation may impart notable alterations to the intrinsic properties of the segmented pattern. Therefore, the segmentation process is initially applied and preserved as the segmented pattern.

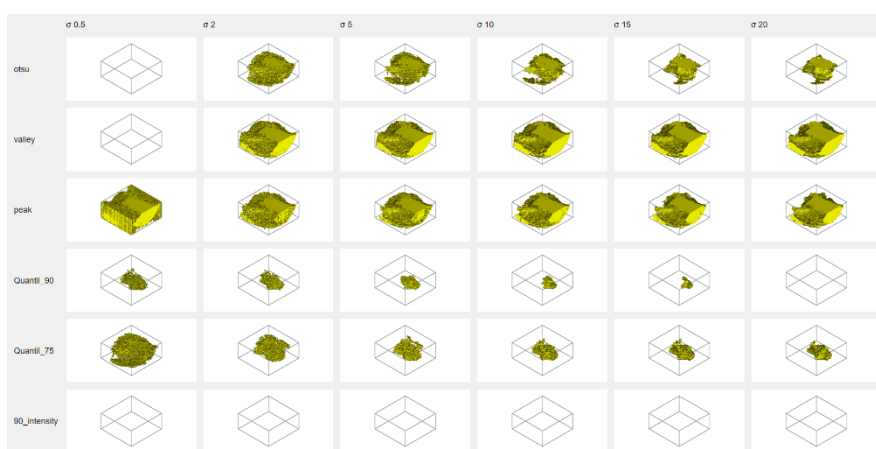


Figure 19: Area open morphological operation on NOGGIN.

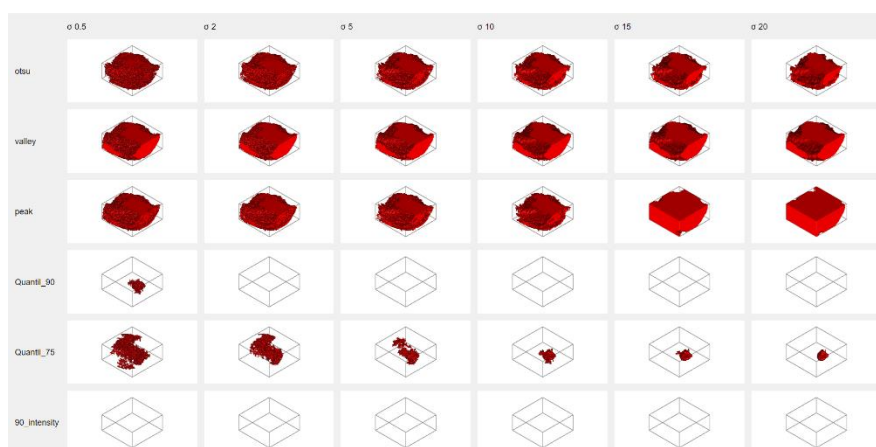


Figure 20: Area open morphological operation on GDF-5.

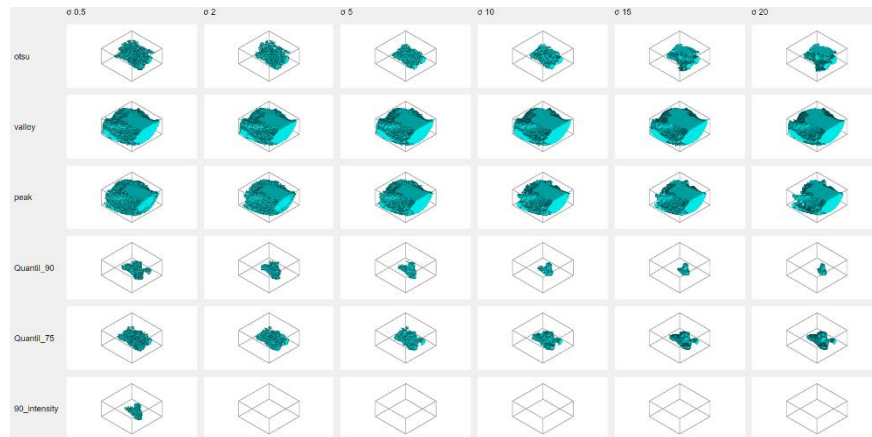


Figure 21: Area open morphological operation on SOX9.

Figure 19, Figure 20 and Figure 21 shows the results for the morphological operation on the images from the previous section, applied to all the possibilities given the binarization thresholds and smooth filter parameters tested.

3.2.4. Segmentation.

The segmentation of the primary pattern is accomplished through a systematic process involving the application of *bwconncomp* and *regionprops3* functions after the *bwareaopen* function. This methodology entails the extraction of interconnected components, referred to as patterns, from the volumetric image. Subsequently, the volume property of these patterns is quantified as volumetric regions.

Following this, the pattern with the greatest volumetric extent is identified (Figure 22, Figure 23 and Figure 24) and designated as the principal pattern segmentation within the possibilities of threshold and sigma smooth parameter. It is worth noting that due to the computational complexity inherent in this procedure, a pragmatic approach is adopted. The images are strategically resized to 50 percent of their original scale at the beginning of the morphological process, after their histogram analysis, utilizing the *makemultilevel* object function of *blockedImage*. This resizing not only optimizes computational efficiency but also safeguards against memory exhaustion.

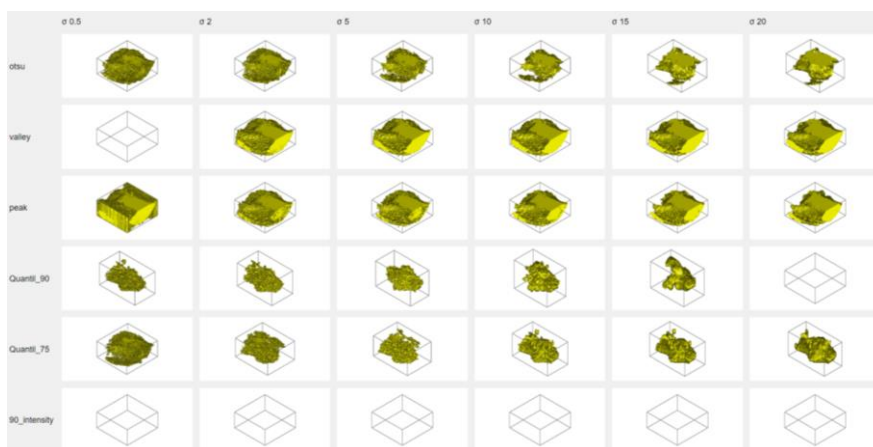


Figure 22: Segmented patterns of NOGGIN.

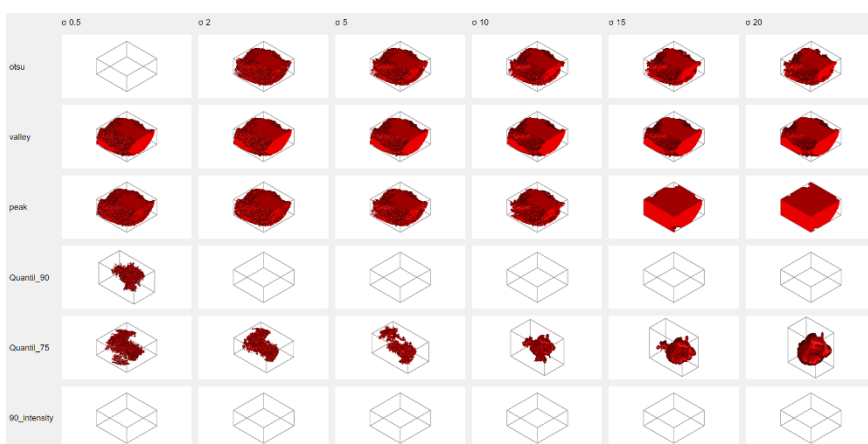


Figure 23: Segmented patterns of GDF-5

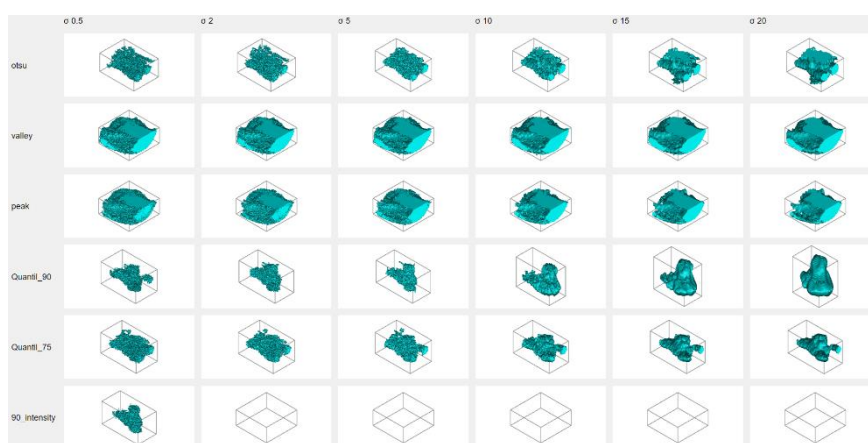


Figure 24: Segmented patterns of SOX9

By executing this well-defined segmentation process, we not only isolate the primary pattern but also ensure that computational constraints are managed, allowing for a comprehensive analysis of volumetric images while preserving memory resources.

3.3. Post – processing

3.3.1. Selection of parameters and segmented pattern.

The criteria for select the best of all segmented pattern, and its threshold and sigma parameters, is done empirical from the observation of the patterns obtained on each morphogen within the same image. It considers that the pattern should be contain without cuts in the capture space, smoothness (non-granularities) of the structure, and insiderness of the pattern.

3.3.2. Measure original properties.

Due to computational constraints, the images were initially scaled down to half of their original resolution level as a preliminary step, prior to accurately quantifying the volumes of retained patterns during the segmentation process. After the extraction and selection of the filled segmented patterns, the *regionprops3* function was reapplied to comprehensively assess their properties. The measurements that are intrinsically affected by resolution change (i.e. volume) were then adjusted by a scaling factor of 2, accounting for the doubled voxel count in the original images compared to the low-resolution segmented ones. Additionally, the property measurements were converted to real-world dimensions by considering the size of each dimension on the voxels, thus facilitating the approximation of the original pattern properties in the physical domain. This methodological approach not only addresses computational limitations but also enables the establishment of meaningful correlations between patterns and their real-world attributes.

With '*VoxelList*' property, the coordinates of each pattern's voxel are acquired. Through the applied conversion to real-world dimensions, these spatial coordinates can be graphed onto unit axes on Figure 25, allowing for an insightful visualization of the pattern distribution in the physical space. With the '*Centroid*' property, geometric center of the pattern, an equivalent reference for translational transformation could be implemented for alignment within images. Also, '*Euler angles*' have the potential to do the same inter image alignment with rotational transformation.

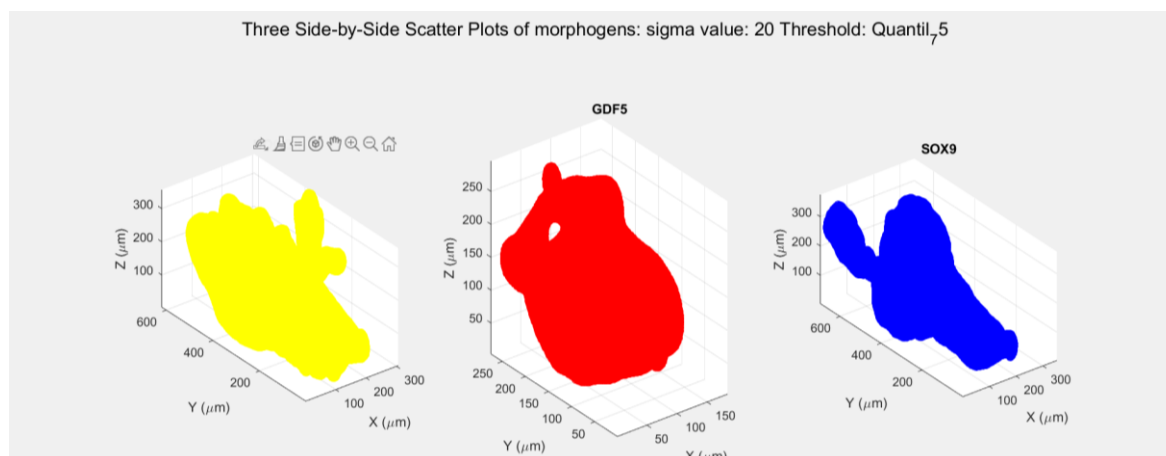


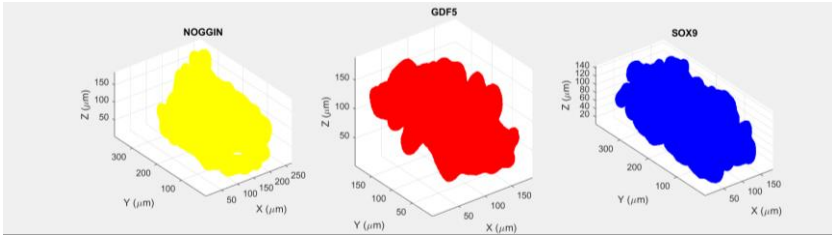
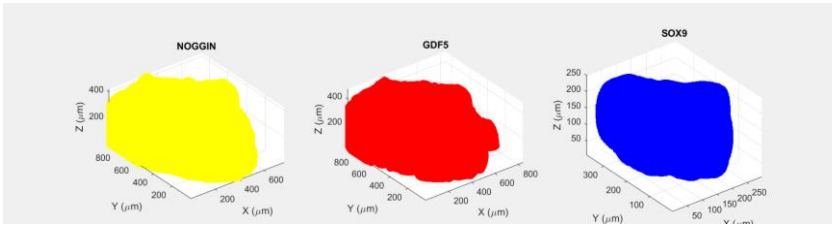
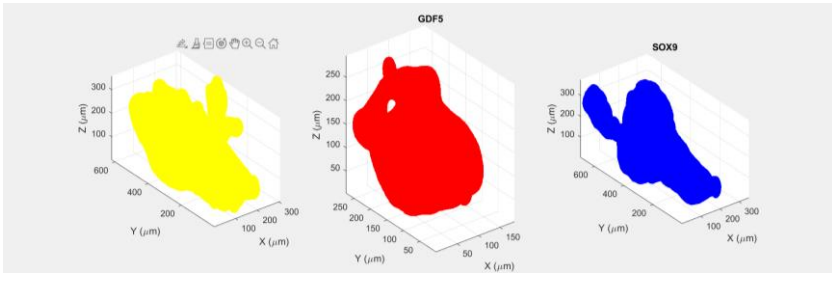
Figure 25: Scatter plot coordinates on real plane.

A total of 18 distinct properties are quantified using the `regionprops3` function within this methodology. Among these, two pertain to the region's own image and its convex hull. An additional two properties involve indices employed for extracting elements within the object's bounding box and the linear indices of the region's voxels. The remaining 14 properties, however, describe the geometric structure of the pattern segmented in the image domain (Voxels), with an approximation of transformation into physical domain. There are: Bonding box, centroid, convex hull, convex volume, Eigen values, Eigen vectors, equivalent diameter, extent, orientation, principal axis length, solidity, surface area, volume, and voxel list.

Evaluating several properties, such as volume, surface area, convex volume, convex hull (which provides the vertex coordinates of the smallest convex polygon that can enclose the region), and the orientation using Euler angles, have potential in describing geometric patterns for parametrization. It is worth noting that caution must be exercised when considering certain properties, such as *'PrincipalAxisLength'* and *'EquivDiameter'* properties that present potential errors due to their translation into physical domain.

4. Results

Table 1 presents the best segmentation coordinates on physical space selected from the observed patterns inside each HCR-FISH microscopy image (Lovely, y otros 2022) available across different days of joint's regeneration. Also, on the column *Filter values* are the process parameters from which the pattern was extracted from the image. All segmented patterns with sigma values and thresholds parameter tested are present in **¡Error! No se encuentra el origen de la referencia.**, from where the present selected patterns were extracted and plot into physical domain.

Post amputation Day	Segmented patterns	Filter values
14		Sigma: 15, Threshold : Quantile 90.
15		Sigma: 20, Threshold Valley.
17		Sigma: 20, Threshold Quantile 75.

<p>18</p>		<p>Sigma: 15, Threshold Quantile 90.</p>
<p>21</p>		<p>Sigma: 15, Threshold Quantile 75.</p>
<p>26</p>		<p>Sigma: 20, Threshold : Quantile 75.</p>

Table 1: Segmented patterns selected.

As the table evidence there are different filter values for the selected segmented patterns, and this most possibly is caused from the nature of *(Fluorescence) in situ hybridization FISH* technique for bind, localizing and detecting specific nucleic acid sequences along with its amplification technique of *hybridization chain reaction HCR* to enhance the sensitivity and signal strength of FISH-based nucleic acid detection. As the images from HCR-FISH complex biological imaging technique can have distinct brightness's levels on which the detection of molecules was made, because of their difference in conditions, reaction and concentration among others, there is not an inter-image standard threshold to be applied in order to segment the desirable pattern observed. But from these results it can be interpreted that a threshold closer to the quantile 75 of the brightness distribution levels values (different to the dynamic range) of the image is a good start to segment the principal high concentrations of molecules. About the sigma parameter variability, is more related to reduce the

“void” between the detected molecules and make a smooth pattern, as the HCR-FISH is a super resolution technique that has the sensibility capability to difference an small amount of molecules from the space (space resolution). The sigma parameter is seemed to behave adequately between 15 and 20 of kernel’s filter size.

PROPERTY	DAY 14	DAY 15	DAY 17	DAY 18	DAY 21	DAY 26
VOLUME	0.0035 mm ³	0.0114 mm ³	0.02 mm ³	0.05 mm ³	0.18 mm ³	0.012 mm ³
SURFACE AREA	0.8 mm ²	0.6 mm ²	1.6 mm ²	2.5 mm ²	4.9 mm ²	1.7 mm ²
CENTROID	X=97 μm, Y=198.1 μm, Z= 74.8 μm	X=136.2 μm, Y=194.4 μm, Z= 127.8 μm	X=144.7 μm, Y= 375.4 μm, Z= 171.7 μm	X=482.2 μm, Y=300 μm, Z=178.9 μm	X=429.6 μm, Y=582.2 μm, Z=350.3 μm,	X=154.6 μm, Y=153.8 μm, Z=229.5 μm

Table 2: SOX9, principal properties; volume, surface area, and centroid.

PROPERTY	DAY 14	DAY 15	DAY 17	DAY 18	DAY 21	DAY 26
VOLUME	0.0018mm ³	0.16 mm ³	0.0045mm ³	0.0062 mm ³	0.09 mm ³	0.0044 mm ³
SURFACE AREA	0.44 mm ²	4.47 mm ²	0.42 mm ²	0.65 mm ²	4.08 mm ²	1.0783 mm ²
CENTROID	X=97 μm Y=88 μm Z=96 μm	X=363.4 μm Y=468.8 μm Z=209.5 μm	X=87 μm Y=146.7 μm Z=120.9 μm	X=270.7 μm Y=165.5 μm Z=180 μm	X=321.8 μm Y=552 μm Z=356.2 μm	X=120.3 μm Y=159.4 μm Z=137.7 μm

Table 3: GDF-5, principal properties; volume, surface area, and centroid

PROPERTY	DAY 14	DAY 15	DAY 17	DAY 18	DAY 21	DAY 26
VOLUME	0.005 mm ³	0.14 mm ³	0.023 mm ³	0.041 mm ³	0.042 mm ³	0.05 mm ³
SURFACE AREA	1 mm ²	4.42 mm ²	1.56 mm ²	3.33 mm ²	1.30 mm ²	4.75 mm ²
CENTROID	X= 147.7 μm Y= 175.7 μm Z= 89.4 μm	X=348.8 μm Y=465.8 μm Z=180.4 μm	X=126.6 μm Y=314.3 μm Z=159.1 μm	X=469.7 μm Y=297.7 μm Z=147.8 μm	X=246.3 μm Y=258.6 μm Z=258.9 μm	X=260.4 μm Y=315 μm Z=252.4 μm

Table 4: NOGGIN, principal properties; volume, surface area, and centroid.

Tables Table 2, Table 3, Table 4 show the image pattern measured properties more relevant: volume, surface area and centroid of the selected patterns from day 14 post amputation to day 26 post amputation of the available image set. Within the remaining properties; Euler angles, eigen values and vectors could also have the potential to quantify and apply transformations to the patterns in order to create a parametrized equation that describe the coordinated locations of the extracted patterns.

Discussion

These results are just an initial step to develop a parametrized equation for each pattern, as these properties could parametrize the self-pattern if an appropriate system of equations is found that correlate each of the relevant properties with the location of the surface points of the pattern. Here, a relevant property is understood as a property bound to the surface points of the volumetric morphogen expression extracted from the image, as there are properties that are not directly dependent on their location (i.e bounding box or convex volume) and therefore they cannot parametrize the pattern itself.

Its worth to mention that the pattern of day 15 post amputation has the worst segmented pattern extraction overall the images, as there is minimal distinction between its morphogen channels, and it also presents a threshold that is distinct from the others. Besides it, the remaining samples show clearly distinct morphogens patterns. This also can be evident in the properties measurements, as the 15 dpa image has the most unrelated properties between the progressive days. From the properties measurements it is possible to interpret that unlike SOX9, NOGGIN and GDF-5 reduce their expression after day 21 post amputation, as their volume and surface area on day 26 post amputation is smaller than day 21 post amputation. Instead, SOX9 keeps expressing continuously as their pattern measurements evidence that on day 26 post amputation continues to grow in volume and surface area. This is expected as SOX9 marks the cartilage production and is use to see the bone rudiments, not been a chemical pathway by itself. This interpretation is done under the assumption that the process of each of the images are the most similar ones to extract the approximated patterns, and measure normalization from images is required for more quantitative comparison. Regarding the extracted patterns into physical coordinate points for each morphogen and image on Table 1, there is still work to do for a proper comparison between days, but these extracted patterns approximates the observations on the images.

These results are just a first step towards the final objective of quantifying the pattern into a parametrized equation, but there are several difficulties to be solved before achieving that goal, which will be discussed next.

Global reference

To ensure accurate comparison among images, alignment is necessary. This alignment involves utilizing properties like Euler angles for rotational adjustment via rotation matrix transformation, centroid calculations for translational alignment by creating translational vectors, and eigenvalues along with eigenvectors to handle more complex linear transformations such as scaling, reflection, and shear.

However, to correlate these transformations across the various images, the presence of a reference point, structure, or object is indispensable. This reference entity should remain fixed and closely associated with the geometric aspects of the pattern, serving as a universal reference across all images. In pursuit of this goal, the utilization of Regions of Interest (ROIs) was explored. Regrettably, implementing ROIs posed difficulties due to the substantial manual uncertainty involved in consistently identifying the same region in all images. Consequently, addressing this matter has been deferred to future endeavors.

Parametrization

The attempt to quantify the patterns involved representing them as three-dimensional equations using MATLAB's curve fitting toolbox to parameterize their surfaces. However, the toolbox could not accurately approximate the patterns as proper three-dimensional equations that could fully define them. This limitation arises from the need for a higher-dimensional solution, which the toolbox does not support. While curve fitting offers various approaches to approximate a group of coordinate points, it primarily interpolates values without providing a parameterized equation or a continuous function that maps the points onto a continuous surface. None of these solutions align with the ultimate goal, which is to find an equation that correlates the coordinates of the surface of the pattern, similar to the equation of a sphere.

It is worth mentioning that this tool also offers models with no parameters, like splines. Another solution explored was the AlphaShape object, a computational geometry tool that represents the bounding region of the pattern and performs calculations based on 2D and 3D geometries. While it allowed useful calculations such as area, perimeter, and volume for comparison and correction, it couldn't directly parametrize the three-dimensional object in the sense of describing it with a mathematical equation. Instead, it serves as a valuable tool for representing and analyzing the shape and structure of three-dimensional point sets, which can be useful for modeling and analyzing 3D objects from discrete data.

Finally, the griddatan technique was also explored and proved to be the most suitable for the objective. It can interpolate N-D data and fit it into a hypersurface in the form of a function that takes sample points and their values as variables. The griddatan function interpolates the surface at specified query points and returns the interpolated values. However, no other tools available in MATLAB could directly address this parametrization problem. Therefore, the need arises to implement mathematical algorithms to parametrize the patterns into a 3D hypersurface, such as numerical methods or Bézier and splines.

Conclusions

The presented methodology outlines the image processing and analysis of morphogen expression images, with a specific focus on NOGGIN, GDF-5, and SOX9. This approach facilitates the extraction of primary concentration patterns and subsequent quantification. Notably, a real physical reference framework has been successfully established, enhancing the practical applicability of the images.

Fourteen distinct properties have been extracted from the images, encompassing a range of geometric parameters and measurements. These properties offer valuable description into the underlying patterns and structures. Of particular importance is the successful characterization of extracted patterns using mathematical descriptors like eigenvalues, eigenvectors, and Euler angles, providing a concise representation of both complexity and orientation.

However, caution is advised, especially concerning surface area properties. This is due to potential systematic errors that may arise during rescaling and transformation into physical space based on voxel resolution.

Pattern selection criteria include factors like smoothness and spatial location within the image space. Challenges persist in alignment and parametrization methods, primarily due to the absence of a universal reference framework for applying transformations to each image. Efforts should be directed toward developing a standardized reference approach to enhance result comparability.

Opportunities for improvement exist, such as refining alignment and parametrization methods independent of a universal reference framework, investigating advanced error mitigation techniques, and exploring the incorporation of brightness relationships among images to improve threshold setting and consistency across different images.

In this work, the focus is on going beyond standard tools like CellProfiler and MIB – microscopy image browser, with the aim of not only segmenting morphogens but also transforming intensity data into real dimensions and parametrizing morphogens concentration patterns. Achieving these objectives involves utilizing MATLAB toolboxes and applying specialized algorithms for data transformation and pattern modelling.

In conclusion, the outcomes of this research not only establish the primary step for validating the model's pursuit of understanding the influence of initial conditions and domain expansion on 3D Turing patterns but also highlight the significant importance and complexity of this exploration.

Economic analysis

For this section, the budget and/or economic analysis associated with the completion of this work is presented. It is important to clarify that this project was purely research-oriented; therefore, it does not involve potential income or indirect costs such as administrative management, permits, and/or insurance. Additionally, to simplify calculations, the value that the acquisition of images could potentially have will be disregarded.

Within the labor category, the hours worked throughout the entire project are considered. A total of 15 hours per week were allocated, starting from the last week of February until September 27, 2023. Therefore, the total number of weeks worked was 30, resulting in a total of 450 hours allocated to tasks such as reading articles and necessary documentation, methodology, testing, corrections, and, finally, report generation.

For budget calculations, the average base salary of a junior engineer (with less than two years of experience) in Spain for 2023 has been used as a reference, as reported by (Talent.com s.f.). This salary is approximately €25,000 annually, equivalent to €12.82 per hour. The following table, labeled as Table 5, displays the breakdown of hours worked for each of the tasks.

Table 5: Budget Breakdown

Tasks and Assignments	Total Hours	Euro per Hour	Total Value
Reading Articles and Documentation	60	12,82€	769,20€
Methodology	120	12,82€	1.538,40€
Testing	60	12,82€	769,20€
Corrections	100	12,82€	1.282,00€
Report Generation	110	12,82€	1.410,20€
Resources	-	-	710€
Total	450	-	6608€ / 5.769€

Within the resources category, a total of €1,488 was allocated, which includes €600 for the average laptop price (Pc componentes s.f.), €90 for RAM memory, €80 for a hard drive, and €69 for a student license of MATLAB (The MathWorks, Inc. 2023). Therefore, the total value of the work, considering only the hours worked, is €5,769, while the total value including both the hours worked and the resources used is €6608.

Ambiental impact

Since this final degree thesis was entirely carried out using a computer, the environmental impact depends on several factors, including the energy efficiency of the computer, the energy source used to power it, and the equipment disposal process at the end of its useful life.

In general, the use of computers for image processing and analysis requires a significant amount of energy. This energy is typically derived from non-renewable sources, such as fossil fuels, which contributes to greenhouse gas emissions and other atmospheric pollutants.

Furthermore, the use of computers and other electronic equipment can generate electronic waste, a substantial portion of which is not properly managed and can have a negative environmental impact through the release of toxic substances.

It is important to mention that to reduce environmental impact, it is necessary to adopt sustainable practices in research work, such as the use of renewable energy and, in the future, responsible disposal of all electronic waste.

Bibliography

- Bankhead, Peter. *Analyzing fluorescence microscopy images with ImageJ*. Belfast: Queen's University Belfast, 2014.
- Besson , S, y otros. «Bringing Open Data to Whole Slide Imaging.» *Lecture Notes in Computer Science* 11435 (2019).
- Brendan F. , Boyce, Zuscik Michael J., y Xing Lianping. «Chapter 11 - Biology of Bone and Cartilage.» En *Genetics of Bone Biology and Skeletal Disease (Second Edition)*, editado por Thakker Rajesh V., Whyte Michael P. y Eisma John A., 173-195. Academic Press, 2018.
- Carl Zeiss, AG. *ZEISS*. s.f. <https://www.zeiss.com/microscopy/en/legal-information/legal-notice.html>.
- Chijimatsu, Ryota, y Taku Saito. «Mechanisms of synovial joint and articular cartilage development.» *Cellular and Molecular Life Sciences*, nº 76 (2019).
- Hofmann, Urs. *GitHub*. 2023. <https://github.com/razanskylab/wavelength2rgb/releases/tag/1.1>.
- Lee, Jangwoo, y David Gardiner. «Regeneration of Limb Joints in the Axolotl (*Ambystoma mexicanum*).» *PloS one*, nº 7 (2012).
- Linkert , M, et al. "Metadata matters: access to image data in the real world." *J Cell Biol.*, 2010 May 31.
- Lovely, Alex, Timothy Duerr, David Stein, Evan Mun, y James Monaghan. «Hybridization Chain Reaction Fluorescence In Situ Hybridization (HCR-FISH) in *Ambystoma mexicanum* Tissue.» 2022.
- Manini, Philip K, Thomas E Woolley, Ruth E Baker, Eamonn A Gaffney, y S Seirin Lee. «Turing's model for biological pattern formation and the robustness problem.» *Interface Focus*, 2012: 487-496.
- Meiniel, William, Jean Christophe Olivo-Marin, y Elsa D Angelini. «Denoising of microscopy images: A review of the state-of-the-art, and a new sparsity-based method.» *IEEE Transactions on Image Processing*, 2018: 3842-3856.
- Otsu, N. «A Threshold Selection Method from Gray-Level Histograms.» *IEEE Transactions on Systems, Man, and Cybernetics*. 9, nº 1 (1979): 62–66.
- Pc componentes*. s.f. <https://www.pccomponentes.com/msi-modern-15-b7m-041xes-amd-ryzen-5-7530u-16gb-512gb-ssd-156> (último acceso: 2023).

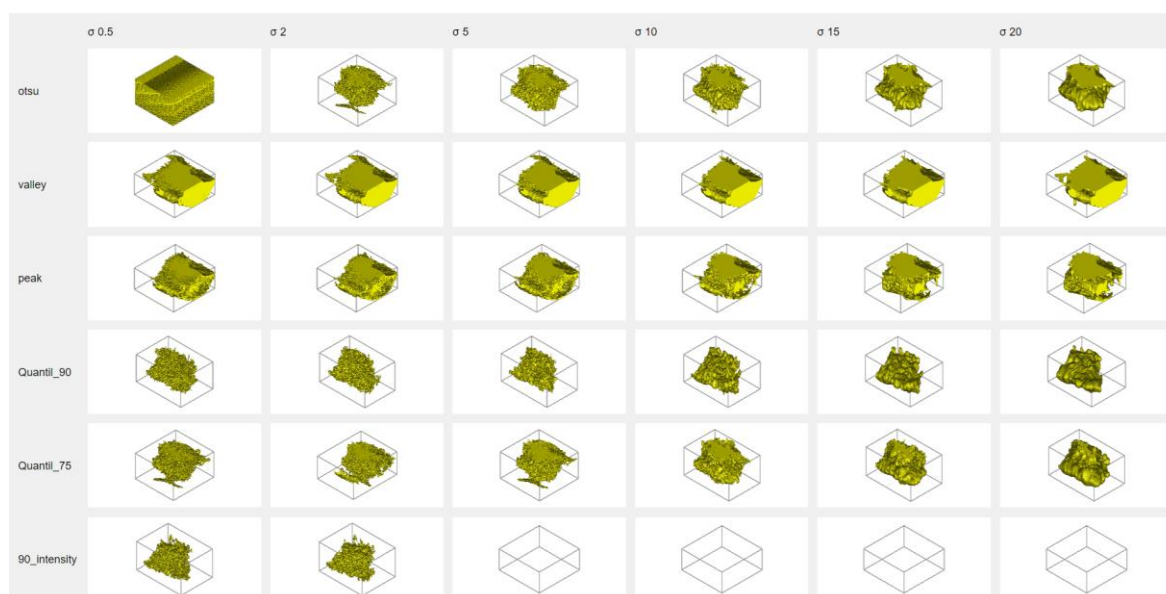
- Schindelin, J., y otros. «Fiji: an open-source platform for biological-image analysis.» *Nature Methods* 7, nº 9 (2012): 676–682.
- Simon, András, y Elly Tanaka. «Limb regeneration. Wiley interdisciplinary reviews.» *Developmental biology*, nº 2 (2013): 291-300.
- Swift, Lucy H., y Pina Colarusso. «Fluorescence Microscopy: A Field Guide for Biologists .» En *Methods in Molecular Biology*, 3-39. 2022.
- Tahar, Soha, Jose Muñoz, Sandra Shefelbine, y Ester Comellas. «Turing pattern prediction in three-dimensional domains: the role of initial conditions and growth.» *bioRxiv*, 2023.
- Talent.com. s.f. <https://es.talent.com/salary?job=Ingeniero+junior> (último acceso: 22 de 09 de 2023).
- The MathWorks, Inc. *apply.* s.f.
https://es.mathworks.com/help/images/ref/blockedimage.apply.html?s_tid=doc_ta.
- . *blockedImage.* s.f. https://es.mathworks.com/help/images/ref/blockedimage.html?s_tid=doc_ta.
- . *bwareaopen.* s.f. https://es.mathworks.com/help/images/ref/bwareaopen.html?s_tid=doc_ta.
- . *deconvblind.* s.f. <https://es.mathworks.com/help/images/ref/deconvblind.html>.
- . *findpeaks.* s.f. https://es.mathworks.com/help/signal/ref/findpeaks.html?s_tid=doc_ta.
- . *imabsdiff.* s.f. https://es.mathworks.com/help/images/ref/imabsdiff.html?s_tid=doc_ta.
- . *imadjustn.* s.f. <https://es.mathworks.com/help/images/ref/imadjustn.html>.
- . *imclose.* s.f. https://es.mathworks.com/help/images/ref/imclose.html?s_tid=doc_ta.
- . *imgaussfilt3.* s.f. https://es.mathworks.com/help/images/ref/imgaussfilt3.html?s_tid=doc_ta.
- . *imsubtract.* s.f. <https://es.mathworks.com/help/images/ref/imsubtract.html>.
- . *interp1.* s.f. https://es.mathworks.com/help/matlab/ref/interp1.html?s_tid=doc_ta.
- . *makeMultiLevel3D.* s.f.
https://es.mathworks.com/help/images/ref/blockedimage.makemultilevel3d.html?s_tid=doc_ta.
- . *Mathworks.* 2023. <https://es.mathworks.com/products/matlab.html>.

Annex

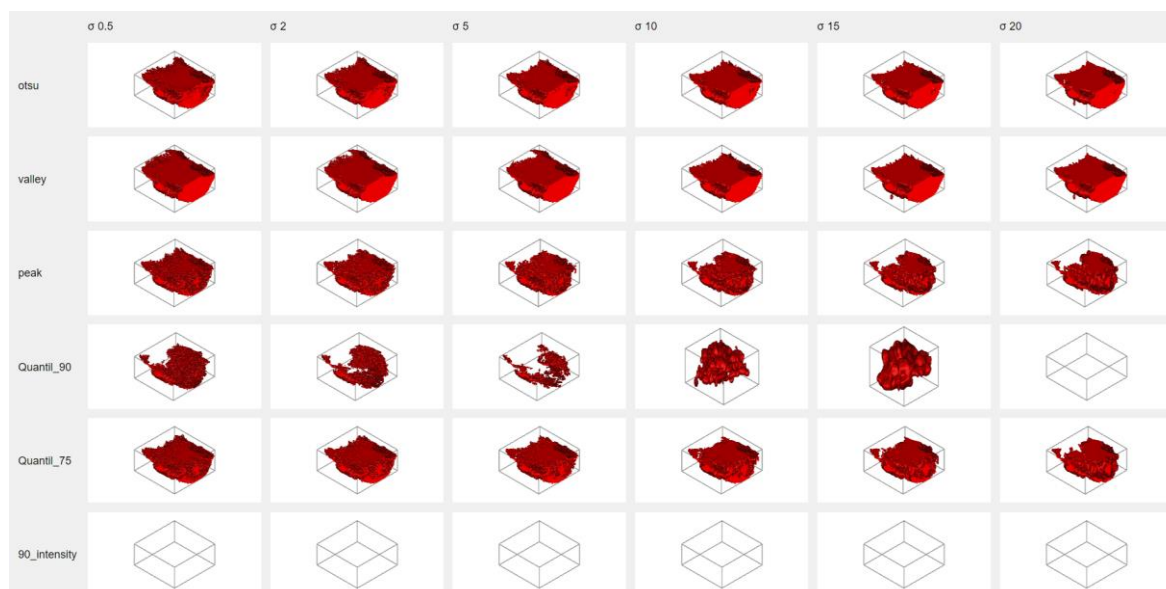
Results for different filter values

Day 14 post amputation

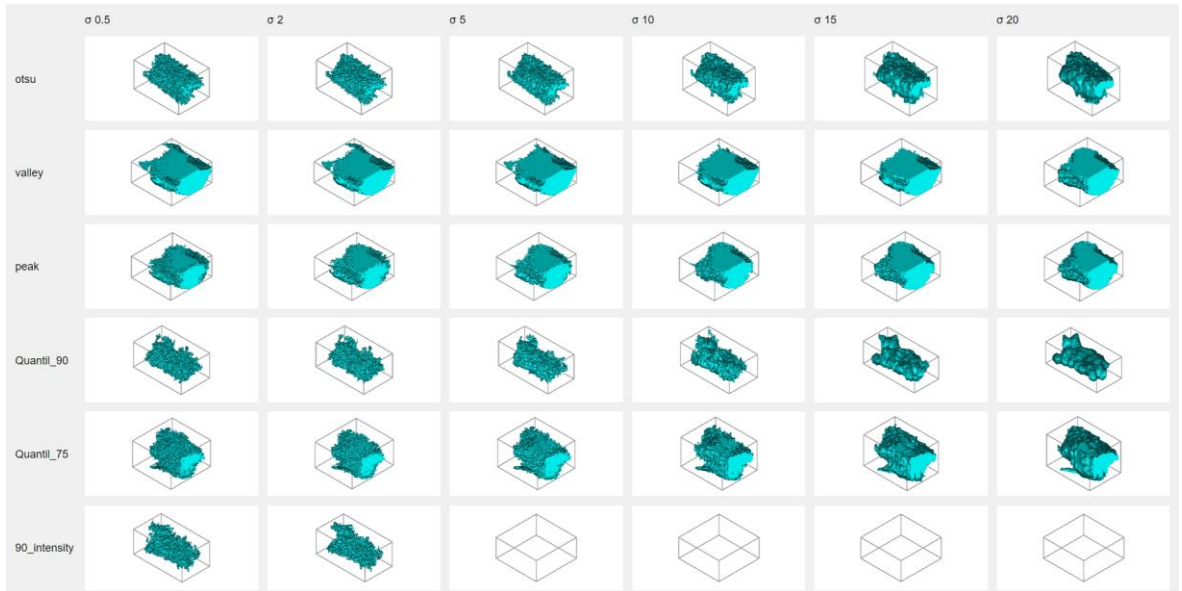
- NOGGIN



- GDF5

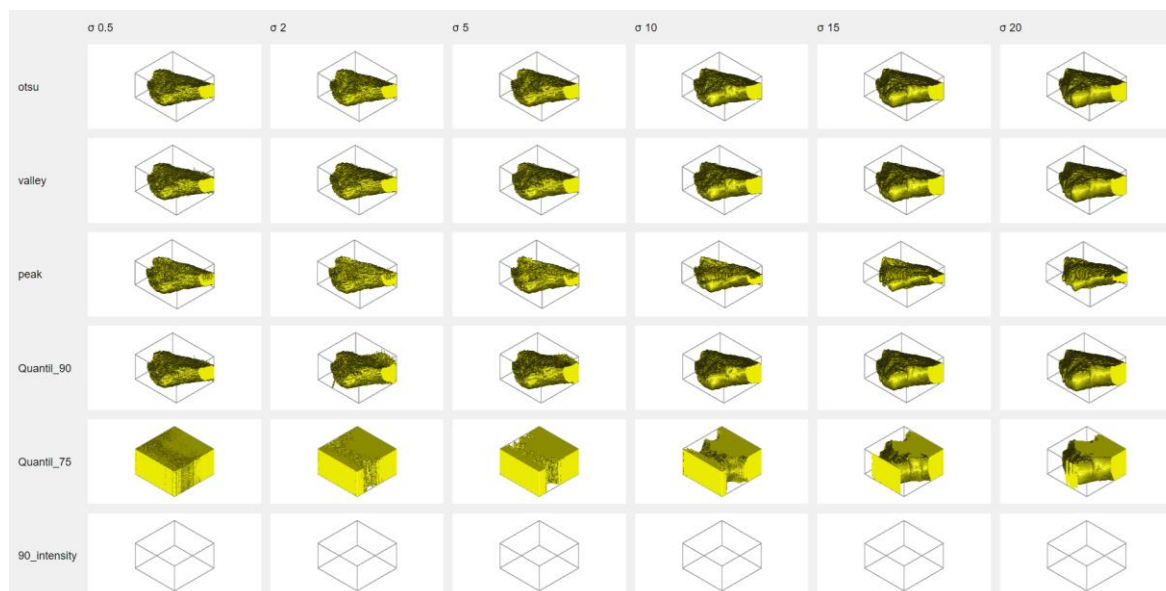


- SOX9

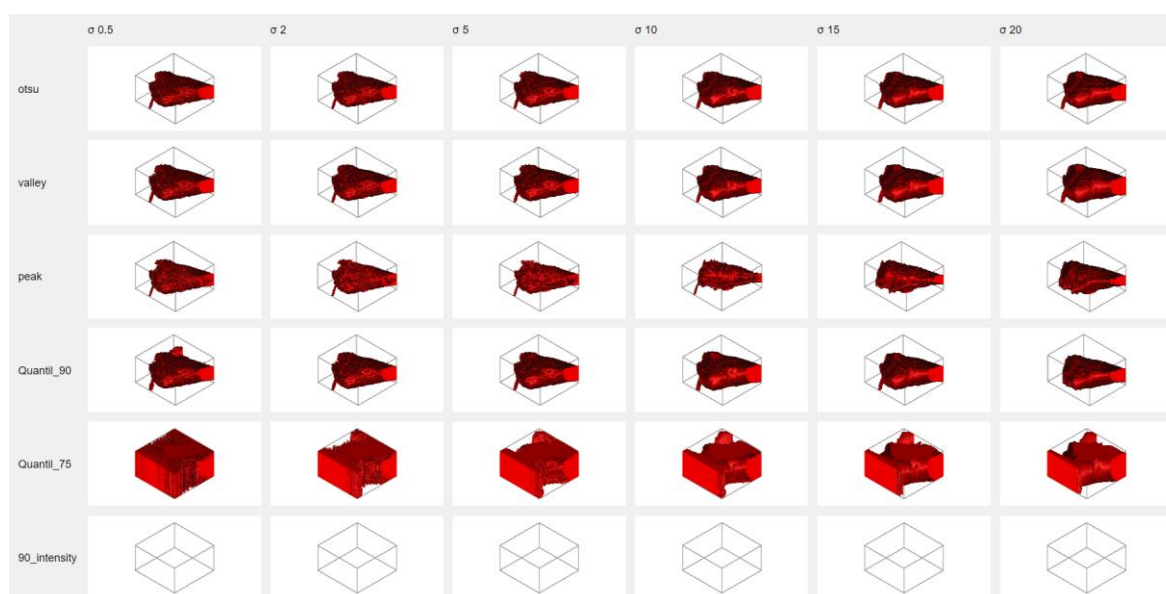


Day 15 post amputation

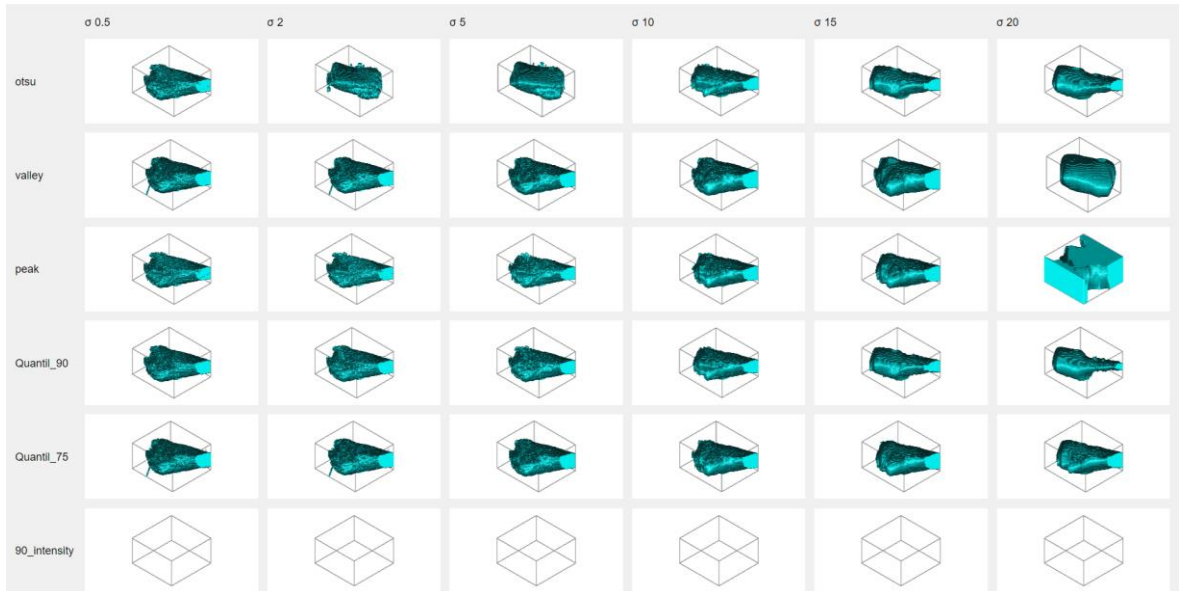
- NOGGIN



- GDF5

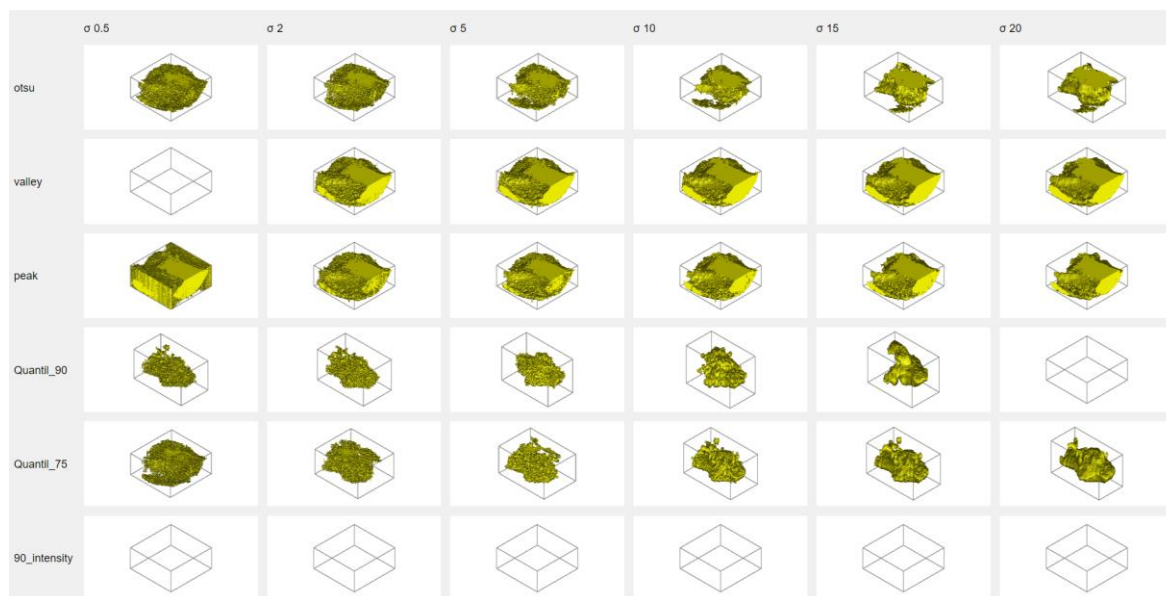


- SOX9

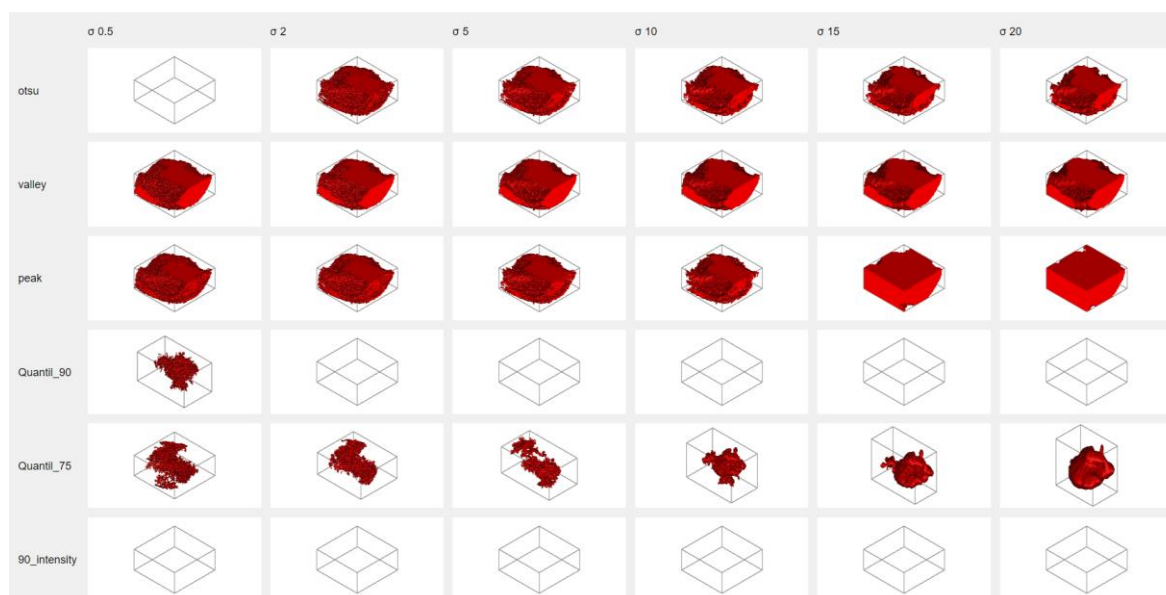


Day 17 post amputation

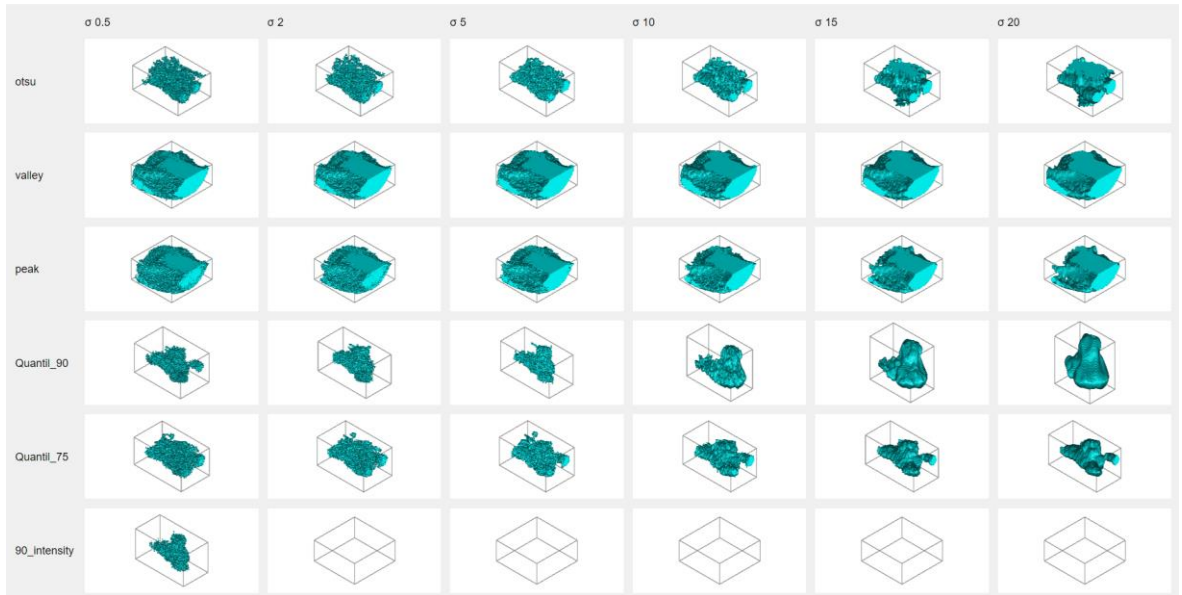
- NOGGIN



- GDF5

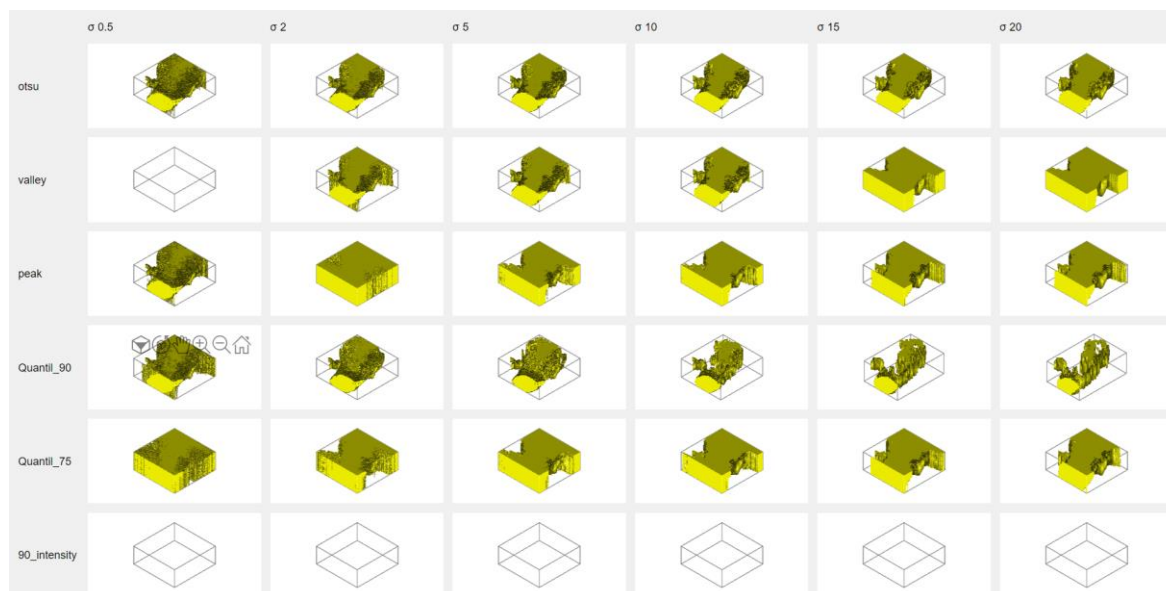


- SOX9

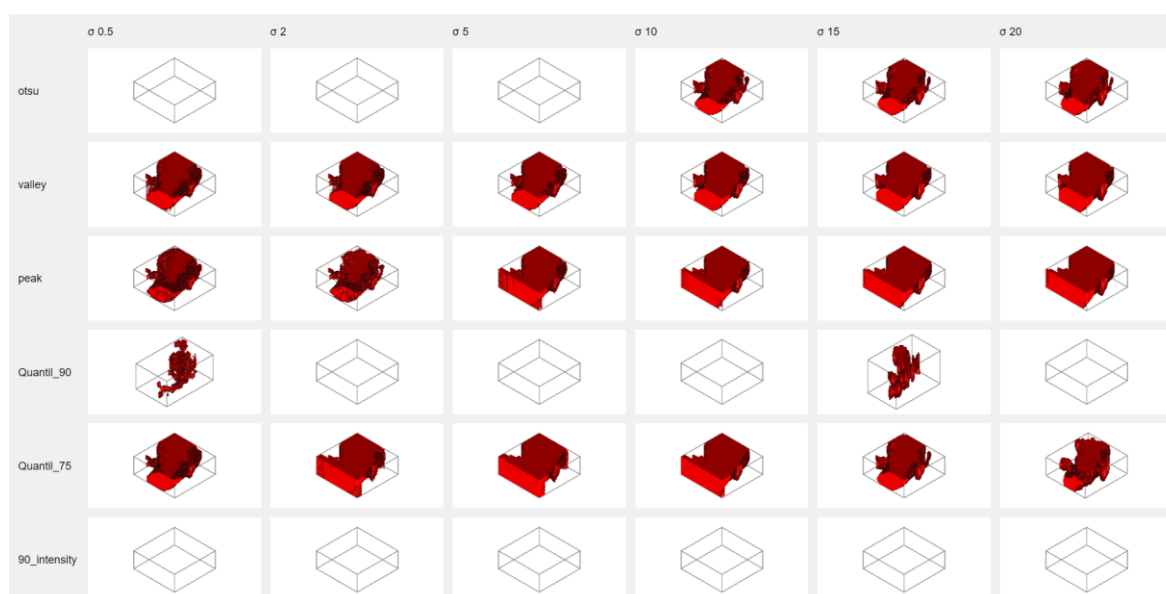


Day 18 post amputation

- NOGGIN

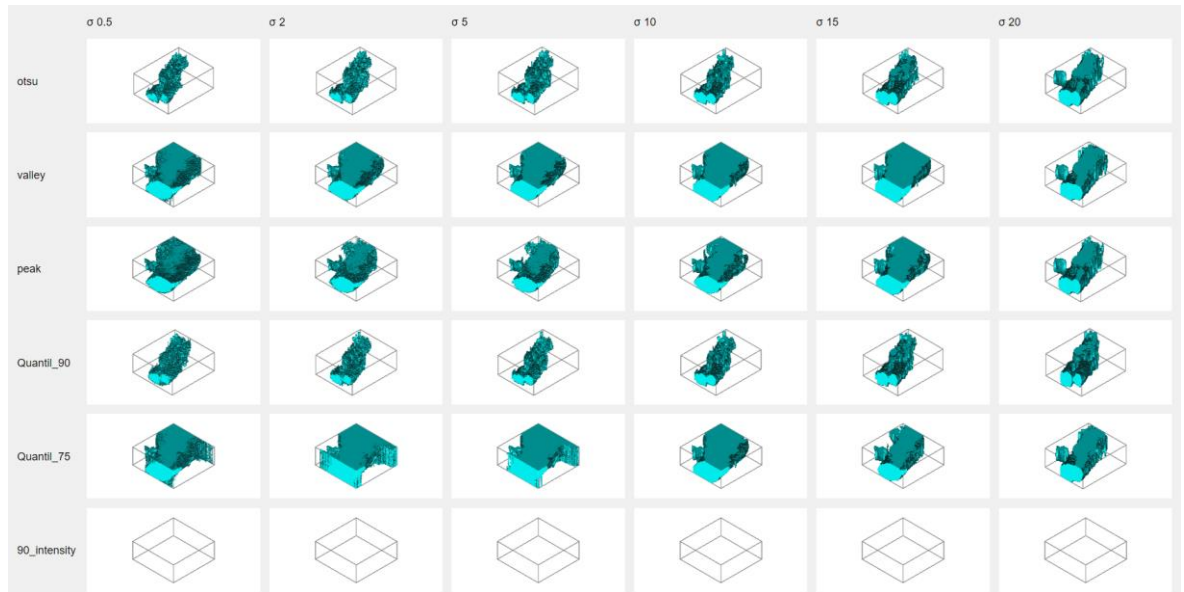


- GDF5



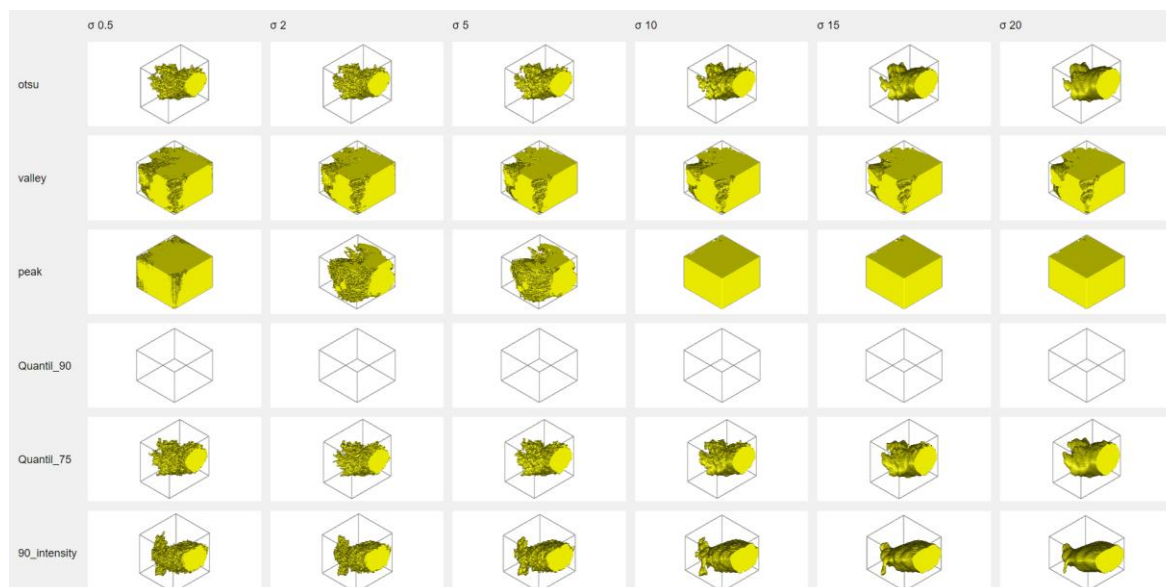
- SOX9

RNA EXPRESSION ANALYSIS AND QUANTIFICATION FROM IMAGES DURING LIMB REGENERATION

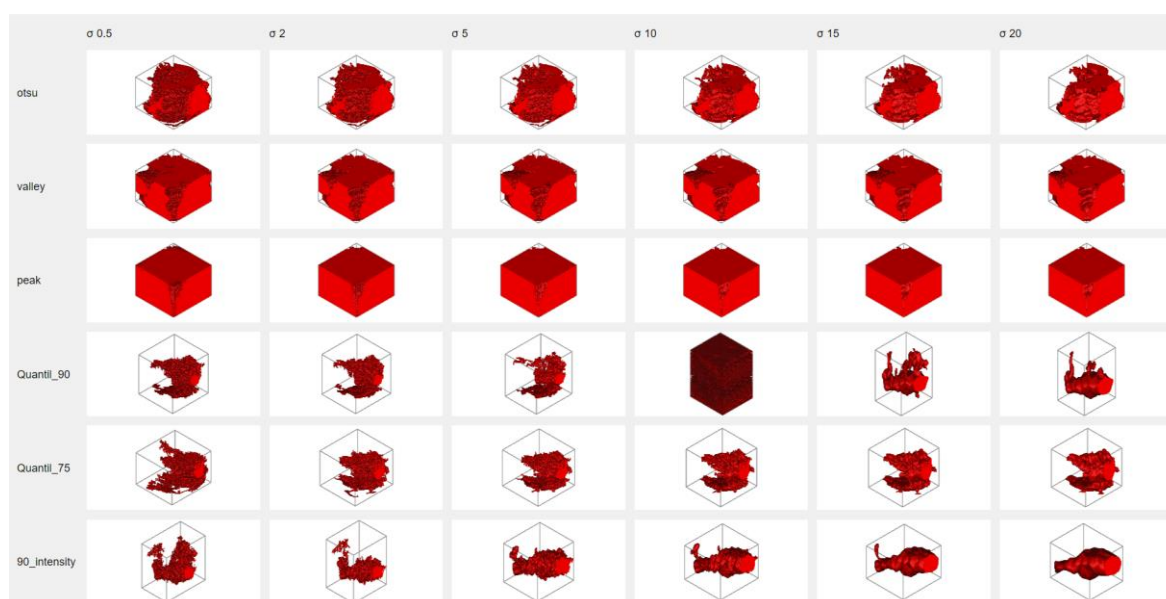


Day 21 post amputation

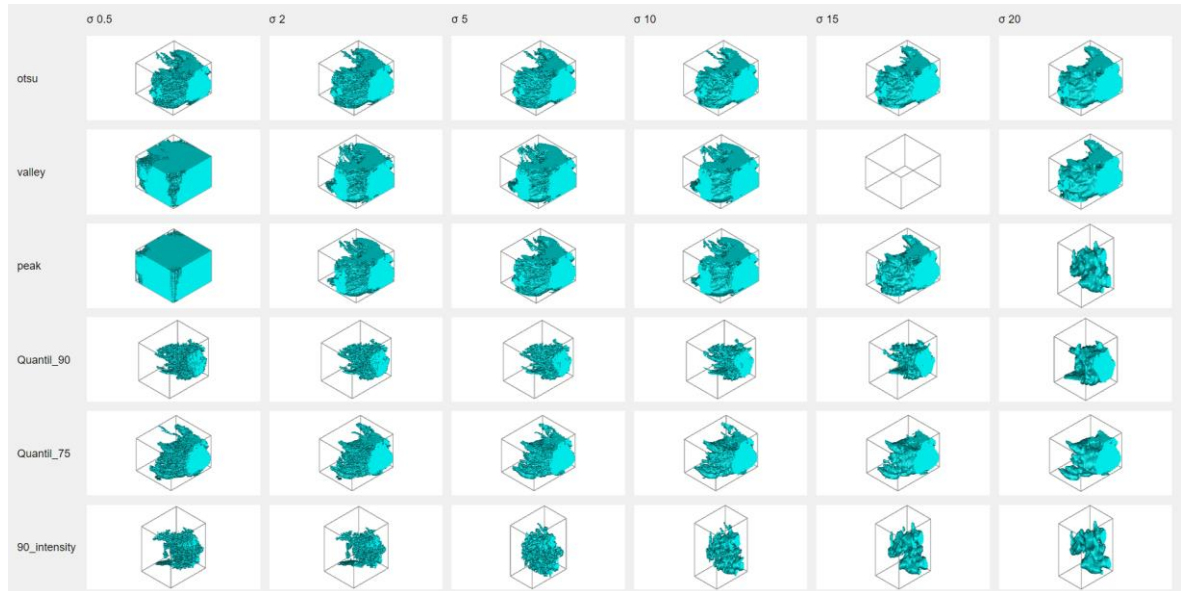
• NOGGIN



• GDF5

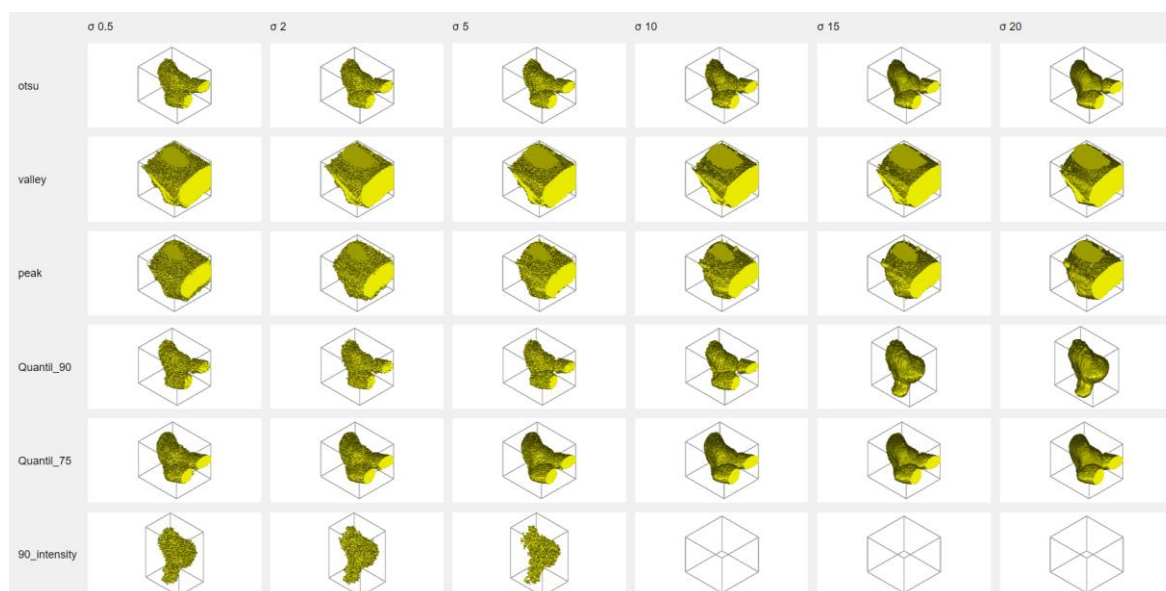


- SOX9

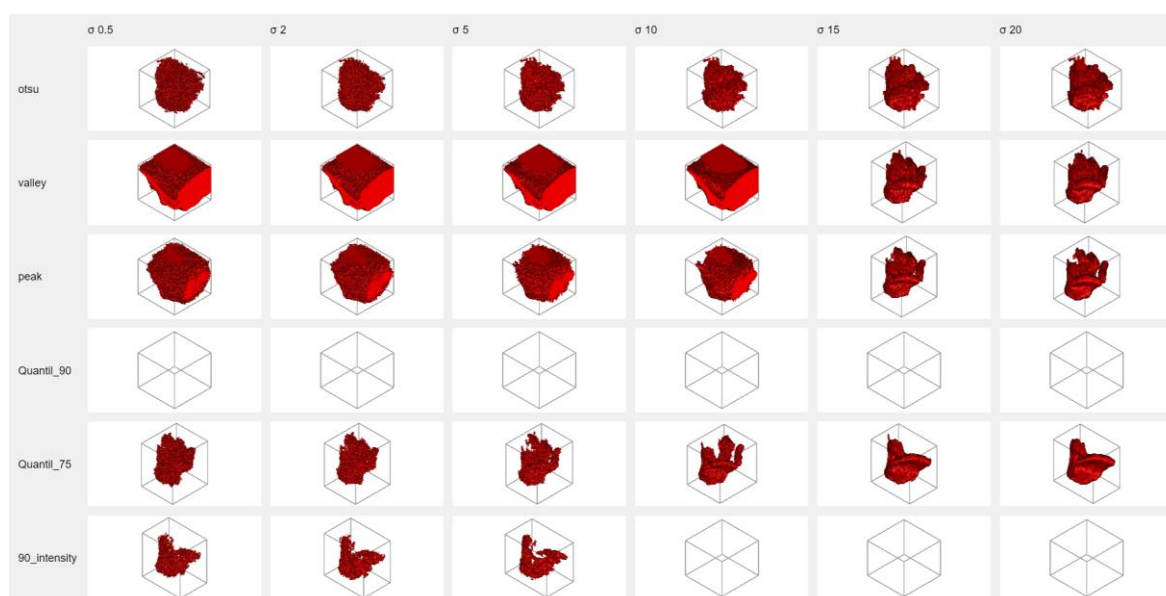


Day 26 post amputation

• NOGGIN



• GDF5



- SOX9

